

Western  Graduate&PostdoctoralStudies

Western University
Scholarship@Western

Electronic Thesis and Dissertation Repository

6-15-2017 12:00 AM

Characterization of an ^{18}F -Growth Hormone Secretagogue Probe for Positron Emission Tomography Imaging of the Growth Hormone Secretagogue Receptor

Ahmed Abbas
The University of Western Ontario

Supervisor
Savita Dhanvantari
The University of Western Ontario

Graduate Program in Medical Biophysics
A thesis submitted in partial fulfillment of the requirements for the degree in Master of Science
© Ahmed Abbas 2017

Follow this and additional works at: <https://ir.lib.uwo.ca/etd>

 Part of the [Animal Experimentation and Research Commons](#), and the [Laboratory and Basic Science Research Commons](#)

Recommended Citation

Abbas, Ahmed, "Characterization of an ^{18}F -Growth Hormone Secretagogue Probe for Positron Emission Tomography Imaging of the Growth Hormone Secretagogue Receptor" (2017). *Electronic Thesis and Dissertation Repository*. 4609.
<https://ir.lib.uwo.ca/etd/4609>

This Dissertation/Thesis is brought to you for free and open access by Scholarship@Western. It has been accepted for inclusion in Electronic Thesis and Dissertation Repository by an authorized administrator of Scholarship@Western. For more information, please contact wlsadmin@uwo.ca.

Abstract

Cardiovascular disease affects 1.6 million Canadians, of whom one-third have heart failure (HF). HF is diagnosed by imaging investigations and detection of circulating biomarkers. Most of the current imaging strategies study morphologic and gross functional changes, but fall short of imaging molecular abnormalities associated with HF. Biomarkers offer molecular targets; however, clinical biomarkers circulate systemically and are not cardiac-specific. Thus, there is critical need for a biomarker that is endogenous to myocardial tissues. The growth hormone secretagogue receptor 1a (GHSR1a), which binds the hormone ghrelin, is expressed by cardiomyocytes and is elevated in HF patients. This study characterized the specificity of the novel tracer [1-Nal⁴, Lys⁵(4-[¹⁸F]-FB)]G-7039 to target GHSR1a using Positron Emission Tomography (PET). *In vitro* analysis of probe specificity by cellular uptake determined that binding was independent of receptor expression, which was confirmed by *in vivo* PET imaging in GHSR1a-wildtype (wt) and -knockout (*ghsr*^{-/-}) mice. *Ex vivo* biodistribution comparing specificity and effects of nutritional state showed that [1-Nal⁴, Lys⁵(4-[¹⁸F]-FB)]G-7039 did not distribute to the heart and uptake was independent of circulating ghrelin levels. Although [1-Nal⁴, Lys⁵(4-[¹⁸F]-FB)]G-7039 demonstrated *in vitro* stability, negligible cardiac uptake and high uptake in the liver, intestines and kidneys within 1 h post-injection indicated rapid probe elimination through hepatobiliary and renal mechanisms, possibly explained by a highly lipophilic tracer. Analysis of cardiac GHSR1a expression and metabolic markers by fluorescence microscopy in fasted, fed, wt and *ghsr*^{-/-} mice suggests that there may be a ghrelin/GHSR1a system in the heart that is regulated independently of systemic ghrelin/GHSR1a, and that GHSR1a does not play a significant role in cardiac metabolism in healthy mice. *In vitro* stability and cellular uptake, *ex vivo* biodistribution and *in vivo* imaging conducted in this study present a step towards characterizing a suitable GHSR1a PET tracer that may be used to detect HF.

Keywords

Heart failure, ghrelin, ghrelin receptor, GHSR1a, PET imaging, GHSR1a knockout mice, GPCR, Cardiac

Co-Authorship Statement

Savita Dhanvantari and Leonard Luyt conceived the study. Savita Dhanvantari and Ahmed Abbas designed experiments. Ahmed Abbas conducted biodistributions, PET image acquisition, and collected samples for and conducted all analyses. Ahmed Abbas was responsible for animal handling and care, statistical analyses, background research, figure and manuscript preparation. Derek Wu performed histological sectioning, staining, and fluorescence microscopy image acquisition and analysis, with contributions from Ahmed Abbas. Lihai Yu and Tyler Lalonde synthesized the tracer and wrote the methods section related to it. Lihai Yu performed all of the tracer injections. Shannon Seney conducted ELISA. Ahmed Abbas, Lynda McCaig, and Karen Nygard harvested and prepared lungs for microscopy. Ahmed Abbas and Tyler Lalonde conducted cell uptake studies together; Tyler Lalonde prepared cells and Ahmed Abbas counted radioactivity. Hilary Groom conducted serum stability experiments.

“Education is our passport to the future, for tomorrow belongs to the people who prepare for it today.”

— *Malcolm X (El-Hajj Malik El-Shabazz)*

Acknowledgments

Thank you, Yuma and Abi for your support and understanding. To my siblings, thank you for picking up my slack; our family operates as a unit, as one body, and while one limb (myself) may be lame from time to time, the others are strong and resilient. I love you deeply.

Savita, thank you for your unparalleled academic support. You've been the key to opening many doors and you've supported me in my many (sometimes crazy) endeavours.

To my labmates, Rebecca, Farzad, and Maya; to the students who worked with us, Derek, Nabeel, and Anne; and to our officemate, Kobra: we've fostered a collegial and amicable environment that has permeated beyond the boundaries of our office and laboratory. Thank you for your friendship and encouragement. Special thanks to Rebecca, because you've been there since day-one and you're always prepared to put up with me.

I acknowledge our collaborators, without whom this project would not be possible. You have provided insight in to potential experiments, suggested improvements, and provided feedback. Thank you to Tyler Lalonde for development of our probe. Special thanks to Dr. Lihai Yu for your professionalism and for coming in several early mornings over many months.

To my advisors Drs Frank Prato and Jonathan Thiessen, thank you for your guidance, suggestions, for challenging me to critically evaluate my work, and especially for helping my project come to fruition. Thank you, Jonathan, for your open-door policy and for providing abundant guidance from your wealth of expertise in PET.

For teaching me and for your patience, laughter, and accommodating me and my "dirty" mice, thank you Jennifer Hadway, Lise Desjardins, and Laura "Deborah/Debbie" Morrison.

To the all the individuals at Lawson and the Medical Biophysics department, you've made my experiences truly enjoyable and memorable. I wish the best for you in the future.

This project was made possible thanks to support from many sources: NSERC, OGS, CIHR, CGS-M, WGRS, and the Western Collaborative Program in Molecular Imaging.

Table of Contents

Abstract.....	i
Co-Authorship Statement.....	ii
Acknowledgments.....	iv
Table of Contents.....	v
List of Tables.....	viii
List of Figures.....	ix
List of Equations.....	x
List of Abbreviations.....	xi
List of Appendices.....	xiv
Chapter 1.....	1
1 Introduction.....	1
1.1 Congestive Heart Failure.....	1
1.1.1 Functional Classifications of HF Evolution.....	2
1.1.2 Etiology and Pathophysiology.....	3
1.1.3 Cardiac Metabolism.....	3
1.2 Diagnosis of Heart Failure and Diagnostic Imaging.....	4
1.2.1 Radiography and Echocardiography.....	5
1.2.2 Cardiac MRI and CT.....	6
1.2.3 Positron Emission Tomography.....	7
1.3 Heart Failure Biomarkers.....	10
1.3.1 RAAS, Natriuretic Peptides, and Cardiac Troponins.....	11
1.4 Ghrelin and GHSR1a.....	13
1.5 Rationale, Motivation, and Previous Work.....	16
1.6 Objectives and Hypothesis.....	18

1.6.1	Specific Aims.....	18
Chapter 2	20
2	Materials and Methods.....	20
2.1	Tracer Synthesis.....	20
2.2	In Vitro Characterization	22
2.2.1	Serum Stability.....	22
2.2.2	Cellular Uptake	22
2.3	Mice	23
2.4	Biodistribution	24
2.5	μ PET and CT Imaging.....	24
2.5.1	μ PET.....	25
2.5.2	Computed Tomography	25
2.5.3	PET Image Reconstruction and Analysis	25
2.6	ELISA	26
2.7	Immunofluorescence Microscopy of Heart and Lungs.....	26
2.7.1	Hearts	27
2.7.2	Lungs.....	28
2.7.3	Microscopy Image Acquisition and Quantification.....	29
2.8	Statistical Analyses	29
2.9	Acknowledgements.....	30
Chapter 3	31
3	Results	31
3.1	Physicochemical Characteristics of [1-Nal ⁴ , Lys ⁵ (4-[¹⁸ F]-FB)]G-7039.....	31
3.1.1	Serum Stability of Unlabeled Probe	33
3.1.2	Cellular Uptake of [1-Nal ⁴ , Lys ⁵ (4-[¹⁸ F]-FB)]G-7039	33
3.2	Ex Vivo Biodistribution in Fasted and Fed Mice	36

3.2.1	Results Post-SOP	36
3.3	Plasma Concentrations of Ghrelin, Glucagon, GLP-1, and Insulin in Fasted and Fed Mice	38
3.4	Heart Immunofluorescence in Fasted and Fed Mice	38
3.5	In Vivo μ PET-CT Imaging.....	41
3.5.1	Time-Activity Curves in wt and $ghsr^{-/-}$ Mice.....	41
3.5.2	Static PET in wt and $ghsr^{-/-}$ Mice	45
3.5.3	Ex Vivo Biodistributions in wt and $ghsr^{-/-}$ Mice.....	45
3.5.4	Heart Immunofluorescence in wt and $ghsr^{-/-}$ Mice	48
3.6	Lung Immunofluorescence in wt and $ghsr^{-/-}$ Mice.....	48
Chapter 4	52
4	Discussion	52
4.1	Physicochemical properties of [1-Nal ⁴ , Lys ⁵ (4-[¹⁸ F]-FB)]G-7039.....	52
4.2	Stability and Cellular Uptake.....	54
4.3	Probe Specificity and Effects of Nutritional State on Binding.....	55
4.4	Circulating Metabolic Hormones.....	57
4.5	Time-Activity Curves	57
4.6	Post-Mortem Tissue Staining of Metabolic Markers.....	58
4.7	Future Directions	60
5	Conclusions and Significance	63
References	64
Appendices	72
Pre-SOP synthesis	74
Biodistributions using Pre-SOP synthesis	74

List of Tables

Table 1. Potential imaging targets early in the evolution of HF.....	7
Table 2. Primary antibodies used for immunofluorescence microscopy.....	28

List of Figures

Figure 1. Chemical structure of [1-Nal ⁴ , Lys ⁵ (4-[¹⁸ F]-FB)]G-7039	32
Figure 2. In Vitro serum stability of [1-Nal ⁴ , Lys ⁵ (4-FB)]G-7039.....	34
Figure 3. Cell uptake of [1-Nal ⁴ , Lys ⁵ (4-[¹⁸ F]-FB)]G-7039	35
Figure 4. Biodistribution profile of [1-Nal ⁴ , Lys ⁵ (4-[¹⁸ F]-FB)]G-7039 using Post-SOP probe synthesis.....	37
Figure 5. Plasma concentration of ghrelin, GLP-1, glucagon, and insulin in fasted and fed mice.....	39
Figure 6. Metabolic profiles of heart samples from fasted and fed mice	40
Figure 7. μ PET-CT imaging in wt and ghsr ^{-/-} mice	42
Figure 8. Heart SUV pattern is similar to lung SUVs.....	43
Figure 9. Time-activity curves for [1-Nal ⁴ , Lys ⁵ (4-[¹⁸ F]-FB)]G-7039 uptake in wt and ghsr ^{-/-} mice.....	44
Figure 10. Static SUVs in wt and ghsr ^{-/-} mice	46
Figure 11. Biodistribution in wt and ghsr ^{-/-} mice.....	47
Figure 12. Metabolic profiles of heart samples from wt and ghsr ^{-/-} mice.....	49
Figure 13. Correlations of cardiac ghrelin expression, heart SUV, and plasma ghrelin with cardiac GHSR1a expression	50
Figure 14. Lung expression of GHSR1a in wt and ghsr ^{-/-} mice.....	51
Figure 15. Compartmental model using a reference tissue to quantify probe flux.....	61
Figure 16. Biodistribution of [1-Nal ⁴ , Lys ⁵ (4-[¹⁸ F]-FB)]G-7039 using Pre-SOP synthesis method in female C57BL/6 mice	75

List of Equations

Equation 1. SUV calculation.....	26
Equation 2. Heart SUV correction	26
Equation 3. [1-Nal ⁴ , Lys ⁵ (4-FB)]G-7039 biological decay	33

List of Abbreviations

%ID/g	Injected dose per gram tissue
ACC/AHA	American College of Cardiology/American Heart Association
ANP	Atrial Natriuretic Peptide
BNP	B-Type Natriuretic Peptide
BSA	Bovine Serum Albumin
CD36	Cluster of Differentiation 36 (AKA Fatty Acid Translocase)
CIN	Contrast-Induced Nephropathy
cMRI	Cardiac Magnetic Resonance Imaging
CO	Cardiac Output
CT	Computed Tomography
cTn	Cardiac Troponin
DIPEA	<i>N,N</i> -Diisopropylethylamine
EC ₅₀	Half-maximal effective concentration
ECG	Electrocardiography
EDC	1-Ethyl-3-(3-dimethylaminopropyl)carbodiimide
EF	Ejection Fraction
ELISA	Enzyme-Linked Immunosorbent Assay
FA	Fatty Acid
FBA	Fluorobenzoic Acid
FDG	Fluorodeoxyglucose
FOV	Field of View
GH	Growth Hormone
GHS	Growth Hormone Secretagogue

GHSR	Growth Hormone Secretagogue Receptor
<i>ghsr</i> ^{-/-}	GHSR knockout mouse model
GLP-1	Glucagon-like Peptide-1
GLUT4	Insulin-dependent glucose transporter
GOAT	ghrelin O-acyltransferase
GPCR	G-Protein Coupled Receptor
H&E	Hematoxylin and Eosin
HED	Hydroxyephedrine
HEK293	Hamster Embryonic Kidney
HF	Heart Failure
IC ₅₀	Half-maximal inhibitory concentration
MAP	Mean Arterial Pressure
NHS	<i>N</i> -Hydroxysuccinimide
NYHA	New York heart Association
OSEM3D	Ordered Subsets Maximization
OVCAR8	Ovarian cancer cell line
PBS	Phosphate Buffered Solution
PET	Positron Emission Tomography
PFA	Paraformaldehyde
Post-SOP	Final synthesis method for [1-Nal4, Lys5(4-[18F]-FB)]G-7039
Pre-SOP	Initial synthesis method for [1-Nal4, Lys5(4-[18F]-FB)]G-7039
RAAS	Renin-Angiotensin-Aldosterone System
RC	Recovery Coefficient
RGD	Arginine-Glycine-Aspartic acid

RPMI	Roswell Park Memorial Institute Medium
SERCA2a	Sarco/Endoplasmic Reticulum Ca ²⁺ -ATPase
SFB	N-Succinimidyl 4-Fluorobenzoate
SUV	Standardized Uptake Value
TPR	Total Peripheral Resistance
VOI	Volume of Interest
wt	Wildtype

List of Appendices

Appendix A. [1-Nal ⁴ , Lys ⁵ (4-[¹⁸ F]-FB)]G-7039 Pre-SOP synthesis method.....	72
Appendix B. Pre-SOP synthesis and biodistribution results.....	74
Appendix C. Animal research ethics approval	76
Appendix D. Primer pairs for genotyping GHSR1a	77

Chapter 1

1 Introduction

Diseases that affect the heart muscle are collectively referred to as cardiomyopathies. The hallmarks of cardiomyopathies include cardiomegaly, heart wall thickening, increased rigidity, ischemia, inflammation, and, in some cases, scar tissue formation. The heart grows weaker as cardiomyopathy escalates, which commonly results in the clinical syndrome of heart failure. Significant advancements in treating and caring for patients with cardiomyopathy, particularly acute myocardial infarction, have reduced incidence of death, leaving survivors susceptible to secondary cardiovascular events and developing heart failure^{1,2}.

1.1 Congestive Heart Failure

Heart failure (HF) is characterized by the inability of the heart to provide adequate cardiac output to meet the metabolic demands of the body. It results in reduced ventricular function. Consequently, the heart is unable to adequately perfuse body tissues because of impaired systolic function (termed HF with reduced ejection fraction, where the ventricles do not eject blood efficiently), diastolic function (termed HF with preserved ejection fraction, where the ventricles are unable to fill effectively) or a combination of the two. This leads to elevated diastolic pressures and fluid backup in the lungs and peripheral tissues. Additionally, kidney function and perfusion is reduced, aggravating fluid backup and further exacerbating fluid retention. The body responds with compensatory measures, including increased heart rate, sympathetic activation, as well as hormonal regulation of blood volume and pressure, such as activation of the renin-angiotensin-aldosterone system (RAAS). Under chronic conditions, HF severity develops marked physiologic and molecular changes, such as natriuretic peptide release and ventricular hypertrophy to raise the force and volume of blood ejected. The congestive nature of HF manifests as chronic fluid retention and increased venous pressure. Patients experience shortness of breath, fatigue, and peripheral edema.

HF generates significant economic burden on the healthcare system and personal challenges for the patients who suffer from it. A cost analysis of the financial burden of admissions for HF between 2004 to 2013 found that admissions where HF is the primary diagnosis place a \$482 M yearly burden on Canadian health services, and these costs are expected to increase to approximately \$722 M by 2030. Accounting for admissions where HF is the secondary diagnosis results in a projected total cost of \$2.8 B in 2030³. HF is also a significant contributor to morbidity and mortality. HF patients have the highest readmission rates of all chronic illness patients in Canada and the second highest readmission volume. Twenty-one percent of HF patients are readmitted to inpatient care within 30 days⁴. Admission rates have increased in the past decade and are expected to continue to increase. It is thought that improvements in therapeutic interventions and management strategies for acute cases contribute to increased survival rates of patients with high probability of developing impaired cardiac function and eventually HF. The incidence rates of HF are also expected to increase in the coming years due to an aging population⁵ and improvements to care that increase survival rates from myocardial infarctions⁶.

1.1.1 Functional Classifications of HF Evolution

The New York Heart Association (NYHA)⁷ classification method is the most prevalent system used to classify HF. It is based on clinical severity and prognosis. The classifications range from mild, asymptomatic HF without limitations to physical activity (stage I) to severe HF with the inability to undergo any form of physical exercise without discomfort (stage IV).

A more recent classification method was devised by the American College of Cardiology (ACC) and American Heart Association (AHA)⁸ which focuses on the evolution of the disease. The ACC/AHA classification system connects risk factors and structural changes to the development of HF. Patients range from stage A, where high risk is present without structural evidence, to stage D, comprising of patients with end-stage disease requiring extensive intervention. Patients in the intermediate stage B have structural dysfunction without symptoms and those in stage C have had or currently have symptoms associated with underlying structural dysfunction. The ACC/AHA classification system emphasizes what others have theorized⁹: that therapeutic action prior to developing structural

aberrations or early in disease evolution (ie. Stages A and B) can reduce morbidity and mortality linked to HF.

Although these methods are popular and reliable for patients, they are limited by the ability of the patient to recognize symptoms and refer to a physician. Moreover, the stages with mild symptoms (NYHA stages I and II) do not present severely enough to motivate medical consultation. Meanwhile, cardiac dysfunction progresses absent intervention.

1.1.2 Etiology and Pathophysiology

HF is a common terminal state of many cardiovascular diseases. Its etiology involves a significant loss of viable cardiomyocytes resulting from damage caused by an insult to the heart. The resultant effect is a reduction in cardiac output, reduced tissue perfusion, and ventricular remodeling that occur over time¹⁰. The most prevalent etiologies are myocyte loss due to myocardial infarction, hypertension, and chronic ischemia. Less common causes include diabetes, bacterial or viral infection, connective tissue diseases, and valvular disease. Some studies have found that a significant portion of patients present with HF of unknown etiology^{11,12}, further underscoring the need to establish an understanding of pathogenesis and pathophysiology.

1.1.3 Cardiac Metabolism

It is established that most HF pathophysiology can be attributed to the body's own compensatory mechanisms^{10,13}. To maintain tissue perfusion caused by decreased mean arterial pressure (MAP) in HF, the body compensates by increasing cardiac output (CO) and/or total peripheral resistance (TPR) through several mechanisms. These include sympathetic autonomic activation, neurohormonal regulation, and ventricular remodeling. Along with hormonal and remodeling changes, molecular aberrations in HF include alterations to Ca²⁺ signaling and altered metabolic pathways.

Cardiac output is a product of the heart rate and the stroke volume (the volume of blood ejected from the heart during systole). Stroke volume is affected by the myocardial stretch during the relaxation phase of the cardiac cycle at the end of diastole (the preload). This relaxation is related to changes in Ca²⁺ signaling in the heart. SERCA2a is an endoplasmic

reticulum-bound Ca^{2+} transporter which shuttles Ca^{2+} from the cytoplasm to the sarcoplasmic reticulum (SR) in cardiomyocytes. The actions of SERCA2a play a role in relaxation, and thus affect the preload. SERCA2a downregulation has been observed in models of HF and patients with HF¹⁴, and potentially contributes to aberrant diastolic function observed in HF patients.

To fuel contractions and ion pumps like SERCA2a, the heart must access appropriate energy sources. Circulating lipids are the primary energy source for cardiomyocytes and are transported into cardiomyocytes via the fatty acid (FA) transporter CD36. CD36 expression is reduced in patients with HF and it has been implicated in contributing to Ca^{2+} handling¹⁵. A reduction in CD36 under chronic ischemic conditions results in changeover from lipids to glucose as the primary metabolic substrate in the myocardium. This is exemplified by upregulation of the insulin-dependent glucose transporter, GLUT4¹⁶. This is especially advantageous under anaerobic conditions, like ischemia, where it is postulated that the switchover is favoured because glucose metabolism is less oxygen-demanding than lipid metabolism¹⁶. These cellular changes occur prior to presentation of outward symptoms in HF patients and provide insight into the molecular progression in the pathogenesis of HF.

Current best practices and interventions fall short of halting or even stalling HF evolution, as shown by a study that found no improvement in prognosis for patients with HF in Ontario over a ten year period¹⁷. Patients continue to deteriorate to the point where cardiac transplantation is necessary or death occurs. Understanding the molecular mechanisms underlying the pathogenesis and pathophysiology of HF could potentially direct the development of novel therapies and diagnostic imaging techniques.

1.2 Diagnosis of Heart Failure and Diagnostic Imaging

Presently, clinicians lack an individual assessment tool to establish a HF diagnosis. Instead, they rely on a combination of resources to definitively diagnosis the condition. Initially, physical examination is coupled with probing into patient history. Clinical diagnosis of HF is limited by non-specific symptoms (which do not always explicitly pertain to the heart), insensitive tests, and few clinical characteristics that make the diagnosis obvious.

Differential diagnoses such as pericardial diseases, liver diseases, nephrotic syndrome, and protein losing enteropathy are possible due to the unspecific nature of the symptoms.

Adjunct to patient history and physical examination, other investigations such as electrocardiography (ECG) can be used to indicate left ventricular hypertrophy or arrhythmias. Major improvements in diagnosis and monitoring have come in the way of imaging investigations, which are employed to document systolic or diastolic dysfunction. Modern HF guidelines call for noninvasive imaging to diagnose disease and guide therapy. The principally applied imaging modalities are radiography and echocardiography.

1.2.1 Radiography and Echocardiography

Radiography and echocardiography are commonly employed imaging tools for identifying changes to structure and function of the heart in the more severe stages of HF. Chest radiography is frequently used to reveal changes to heart shape and size, along with characteristics of excess fluid, such as pulmonary congestion and pleural effusion. Echocardiography is a powerful tool used in diagnostic imaging of HF to evaluate ventricular size and identify valvular dysfunction and abnormalities¹⁸. Echocardiography also affords clinicians the ability to measure ejection fraction to indicate systolic function. Both are relatively low-cost techniques and widely available in clinical settings.

These methods are useful in their sensitivity and predictive power, but they are only particularly adept when a patient is experiencing physical discomfort (ie. NYHA stages \geq II; ACC/AHA stage \geq B) and presenting outward symptoms. Echocardiography requires expert acquisition and has high potential for intra-observer variability. Two-dimensional echo requires imaging in the appropriate axis, and radiography also only provides a two-dimensional shadow; imaging a three-dimensional object in two-dimensions reduces quality measurements and the amount of information that can be obtained in an investigation. There are several three-dimensional imaging modalities under active investigation for application in imaging heart failure. Recent advances have been made in Cardiac Magnetic Resonance Imaging (cMRI), Computed Tomography (CT), and Positron Emission Tomography.

1.2.2 Cardiac MRI and CT

cMRI is a recent development in imaging heart failure and is being championed for recovering early structural information regarding cardiomyopathies (ACC/AHA stage B). It is a powerful diagnostic tool whose images provide three-dimensional information about heart size, ventricular wall thickness, and functional (regarding ejection fraction in particular) and morphological information. The latter two are especially significant in allowing one to distinguish between health and disease¹⁹. Clinically, gadolinium contrast can be applied to enhance images and aid in imaging myocardial fibrosis²⁰. This method, however, is unable to detect diffuse fibrosis, which is notable because in ischemic cardiomyopathy, there is more diffuse than regional fibrosis²¹. To address this, techniques using T1 mapping prior to and after contrast enhancement have been used to reflect diffuse fibrosis²². Unfortunately, cMRI with gadolinium-based contrast is limited to patients who do not have implantable devices²³ and is also contraindicated in those with advanced kidney disease, a common comorbidity seen in HF patients. Without contrast, there are limitations in quantification because cMRI is primarily an anatomic imaging modality.

An alternative technique is CT imaging, which has seen clinical applications since the 1970s and provides high resolution morphologic and anatomic information, thus allowing good visualization of gross anatomy. Contrast can also be used in coronary angiography for visualization of arterial stenosis. Studies are currently being conducted in imaging of myocardial perfusion to evaluate myocardial blood flow and cardiac lesions resulting from coronary artery disease. In comparison with the other techniques mentioned, CT lacks strong evidence in HF application²³. Also, contrast CT must address safety issues surrounding radiation exposure and risks for contrast-induced nephropathy (CIN) because patients categorized into NYHA class \geq II and with low glomerular filtration rates (including patients with HF) are susceptible to CIN²⁴.

Although the clinical techniques discussed are adept at providing morphological details and characterizing overall cardiac function in HF patients, they have marked detection limitations and are not yet equipped to predict on-set of HF prior to overt symptoms. Also, these modalities are used for diagnosis when HF is already established. Results from other imaging strategies that look at questions surrounding etiology, severity, and reversibility

are important, such as the targets described in Table 1 below, and can facilitate targeted interventions. One clinical imaging modality that can detect biochemical changes early in the pathogenesis of HF and potentially provide answers to these questions is Positron Emission Tomography (PET).

Table 1. Potential imaging targets early in the evolution of HF

ACC-AHA /NYHA Stage	IMAGING TARGETS	
	Pathogenic Event	Possible Imaging Targets ²⁵
A/None	Left ventricular hypertrophy and remodeling	Microvascular perfusion imaging: endothelial function and activity
	Atherosclerosis	Imaging plaque deposition: calcification, apoptosis, fibrosis
	Ischemia	Myocardial perfusion imaging
	Myocardial infarction (MI)	Post-MI imaging of myocardial injury: apoptosis, fibrosis, inflammation
	Ventricular dysfunction	Neurohormones of RAAS
B/I	Remodeling and ventricular enlargement	Remodeling and ventricular enlargement: structural damage whilst asymptomatic Myocardial metabolism and perfusion: FA uptake, glucose uptake, and flow reserve

1.2.3 Positron Emission Tomography

PET is a powerful technique for non-invasive and quantitative visualization of the *in vivo* distribution of a radioactive isotope (such as ¹¹C, ¹³N, ¹⁵O, ¹⁸F, ⁶⁸Ga, and ⁸²Rb) integrated into a biologically relevant molecule. It provides modest spatial resolution and high sensitivity. Positron-emitter labeled compounds are useful for drug development and assessing cellular uptake based on gamma-ray counting. PET is sensitive enough to detect

very low concentrations of injected tracer (10^{-11} - 10^{-12} M)²⁶. Radiotracers commonly used in PET target known biochemical pathways that are the basis for metabolic processes, such as oxygen consumption and glucose and FA transport.

For clinical HF imaging, PET is primarily used for imaging ischemia and myocardial viability²⁷. Identifying ischemia in HF patients is important for prognostic information and will inform therapy decisions. Ischemia is evaluated using perfusion studies that measure intracardiac blood flow and flow reserve, allowing for assessment of the functional impact of coronary artery disease in HF²⁸. A study in patients with chronic ischemic heart disease used ¹³N-ammonia and ¹⁸F-FDG to measure the effectiveness of PET-myocardial perfusion imaging in predicting HF outcomes and discovered that perfusion reserve was a better indicator of death than ejection fraction (EF), which is a measurement of cardiac function commonly obtained using echocardiography²⁹. Perfusible tissue fraction can also be observed using ¹³N-ammonia and C¹⁵O-PET and PET perfusion imaging has been used to distinguish patients with dilated cardiomyopathy of unknown etiology^{30,31}.

The most commonly used PET tracer is ¹⁸F-fluorodeoxyglucose (¹⁸F-FDG), first synthesized by Ido et al³². ¹⁸F-FDG detects glucose metabolism and accumulates in metabolizing tissues. It is the current clinical standard for detecting regional myocardial viability and can accurately identify viability and predict functional recovery³³.

Although imaging ischemia, perfusion, and viability are important in established HF, the power of PET can be utilized to detect changes that occur in pathogenic mechanisms of HF and to study the molecular changes underlying pathophysiology, which can be used to monitor disease progression and to evaluate therapeutic targets and drug efficacy.

Recent developments in PET imaging of HF target molecular pathways like sympathetic innervation and cellular processes in cardiac tissue^{34,35}. Because the autonomic nervous system contributes heavily to the pathophysiology observed in HF, labeled neurotransmitter PET tracers like [¹¹C]hydroxyephedrine (¹¹C-HED) and [¹¹C]epinephrine have been used to measure the density of sympathetic nerve terminals^{36,37}. ¹¹C-HED demonstrated fast blood clearance and high heart distribution. Heart transplant patients had significantly lower retention compared to healthy volunteers, suggesting probe sensitivity

to neuronal activity. Another tracer, ^{11}C -CGP12177, targets β -adrenoreceptor expression in the myocardium and showed reduced receptor expression in patients with dilated cardiomyopathy³⁸. ^{11}C -CGP12177 was able to predict treatment response by detecting myocardial β -adrenoreceptor density, while echocardiography could not³⁹. This emphasizes the potential of PET in evaluating regional molecular changes. Probes that target the nervous system can help guide pharmacological therapies that exert their effects on cardiac autonomic sympathetic activity and can reveal insight into pathophysiological mechanisms⁴⁰.

Several targets are currently being studied for cardiac molecular imaging using PET. These include imaging cellular apoptosis using ^{18}F -Annexin V and ^{68}Ga -Annexin V²⁵, and imaging angiogenic mechanisms involved in remodeling such as the integrin $\alpha_v\beta_3$ (with ^{18}F -arginine-glycine-aspartic acid – ^{18}F -RGD)⁴⁰.

Apoptosis is a major mechanism of cardiomyocyte death in HF⁴¹ and subsequent development of HF. Annexin V binds phosphatidylserine which is a phospholipid that is exposed to the surface in apoptotic cells. Use of ^{18}F -Annexin V has been reported in detection of myocardial ischemia and reperfusion injury in rats⁴². They described specific cardiac localization and greater uptake in hearts of reperfusion injury rats. Another study described differential cardiac uptake of ^{18}F -Annexin V in MI-induced mice with administered Parathyroid Hormone Treatment as compared to controls, while ejection fraction was unable to reveal differences⁴³. ^{18}F -Annexin V showed promise as an apoptosis-targeting tracer and, coupled with its short physical half-life and quick clearance through the urinary system, it showed potential clinical utility. However, accumulation and slow clearance in the liver hinder transition to the clinic so further development and validation is needed.

Angiogenesis occurs following MI and is involved in ventricular remodeling. Integrins are involved in the angiogenic process. The tracer ^{18}F -RGD is used to target $\alpha_v\beta_3$, a plasma membrane glycoprotein receptor that mediates angiogenesis and is highly expressed in activated endothelial cells^{25,44}. ^{18}F -RGD has shown increased uptake in a rat model of MI prior to ventricular remodeling⁴⁵, showing that $\alpha_v\beta_3$ is a possible marker of vascular

remodeling/angiogenesis early in the repair process. ^{18}F -RGD has also seen clinical application⁴⁶, but requires further investigation. Future investigations should also consider $\alpha_v\beta_3$ specificity because there are many biochemical pathways (hypertrophy, inflammation, wound healing, fibrosis) that involve integrins and cell types (fibroblasts, cardiomyocytes, and vascular cells) that express integrins.

These techniques have potential in guiding personalized therapy, which will allow individual disease management to facilitate better outcomes for patients with HF. In spite of these promising developments, HF is molecularly complex so there is still need for development of radiotracers to image changes and distinguish various biochemical pathways that can elucidate between benign changes and disease. None of the mentioned tracers can individually make these distinctions reliably. Biomarkers are a useful pursuit to obtain a more complete understanding of HF.

1.3 Heart Failure Biomarkers

Methods of identifying individuals with high risk of developing HF are urgently needed, especially in the early stages of HF when clinical status and heart function are poor predictors of clinical outcomes and disease stratification. After the syndrome is identified, methods to monitor therapeutic response would be useful.

Biomarkers are objectively quantifiable indicators of biological processes. Elucidating biomarker profiles of HF will prove useful in guiding management and therapy, and potentially revealing the molecular mechanisms underlying the initial stages of cardiomyopathy. Some ideal qualities of a cardiac biomarker for chronic injury are:

- Provides accurate and repeatable measurement
- Present in the heart at an early stage of pathogenesis
- Cardiac specificity, where it is intrinsic to heart tissue
- Highly sensitive, where it can report changes in cardiac function

- Chemically stable, where its quantity peaks to detectable levels and is not degraded before measurements can be made

Currently, natriuretic peptides are clinically validated and established for investigating and monitoring HF, and other biomarkers are under active investigation for potential use.

1.3.1 RAAS, Natriuretic Peptides, and Cardiac Troponins

The physiologic compensatory measures in HF are generally considered to be biomarkers of HF¹⁰. As discussed in the Cardiac Metabolism section (1.1.3), these processes are intended to maintain the heart's mechanical function and tissue perfusion by regulating CO and TPR. Some biomarkers indicate intracellular changes in cardiomyocytes relating to stress and injury (BNP and cardiac troponins), which reduce CO. Others include neurohormones (BNP, NT-ProBNP, ANP, renin/angiotensin II) that affect TPR.

In the early stages of HF, neurohormonal activation contributes to maintenance of tissue perfusion partly by increasing TPR. One pathway that is activated is the renin-angiotensin-aldosterone system (RAAS). In RAAS, the enzyme renin is secreted by the kidneys in response to reduced renal perfusion when MAP is decreased. Renin cleaves angiotensinogen to form angiotensin I, which is converted to angiotensin II by angiotensin-converting enzyme (ACE). Angiotensin II increases vasoconstriction, thereby increasing TPR, and promotes aldosterone release, which causes sodium retention. The net effect is an increase in blood volume and MAP. RAAS has a fundamental role in the pathogenesis of the renal and cardiovascular symptoms of HF¹⁰. Renin, angiotensin II, and aldosterone are targeted in HF management using ACE inhibitors and angiotensin-receptor blockers⁴⁷, and are actively being investigated as biomarkers of HF⁴⁸⁻⁵⁰. In acute circumstances, activation of RAAS is useful in compensation for decreased MAP, which is thought to be why it is active in the early stages of HF. However, long term-activation leads to ventricular remodeling, further deteriorating heart function.

The natriuretic peptide (NP) family partly consists of the hormones atrial natriuretic peptide (ANP) and B-type natriuretic peptide (BNP). They are thought to play a protective role in HF because they counteract the effects of chronic neurohormonal activation;

whereas RAAS results in vasoconstriction, fluid retention and sodium reabsorption (which leads to congestion/volume overload), NPs vasodilate, stimulate natriuresis and diuresis (sodium and water excretion), and inhibit renin and aldosterone production⁵¹. ANP and BNP are eliminated by two pathways: receptor-mediated internalization and metabolism, and proteolytic degradation in the kidneys, vascular endothelium, lungs, and the heart. ANP is cleared more quickly through both pathways. As a result, its biological circulating half-life (3-5 min) is approximately 5-times shorter than BNP's (~23 min) – which is even shorter than the half-life of BNP's N-terminal fragment, NT-proBNP (60-120 min)⁴⁷. Comparisons of diagnostic performance between ANP and BNP support the use of BNP so most clinical diagnostic tests employ BNP and NT-proBNP as circulating biomarkers of HF⁵².

ANP is secreted by the atria of the heart in response to hypertension and wall stress caused by increased blood volume. BNP and NT-proBNP are also markers of volume load and wall stress. The use of BNP and NT-proBNP is established as a standard to rule out HF, as recommended by the Canadian Cardiovascular Society's Heart Failure Management Guidelines¹⁸. However, comorbidities are confounding variables and must be accounted for when measuring BNP levels. Circulating BNP is reduced in obese patients⁵³ and patients with renal failure and HF have elevated plasma NT-proBNP⁴⁸. Both compounds are elevated with age and differ based on sex^{54,55}. A study in 558 patients with chronic HF found that BNP levels varied with age and renal function⁵⁶. Notably, they also observed large variations in asymptomatic patients (NYHA class I) with values ranging beyond clinical cutoffs for more severe diagnosis. One-fifth of patients studied with symptomatic HF (NYHA class II or III) had levels less than the median value observed in asymptomatic patients. The results suggested that BNP levels in HF could also depend on yet unknown factors as well as disease severity and genetic polymorphisms⁵⁶. With such variability, it has been postulated that using circulating BNP levels may be unsuitable in HF management⁴⁷.

Cardiac troponins (cTns) T and I are leading candidates in the search for novel HF biomarkers⁵⁷. They are well established as biomarkers for myocardial injury and are historically used to diagnose myocardial infarction. cTns are markers of remodeling

associated with myocyte injury and death and have shown utility in diagnosis and prognosis in HF⁵⁸. Serial measurements are used as predictors of cardiac remodeling. Unfortunately, there are several conditions where cardiac troponin levels are elevated including hypertension, myocarditis, cardiac amyloidosis, and hypertrophic cardiomyopathy⁵⁹. Moreover, remodeling occurs in the later stages of HF which does not provide adequate appraisal of HF development.

Although simple blood tests can be used to detect the circulating biomarkers discussed, many of these compounds are not specific to cardiac tissue and are produced by several tissues in response to injury or when heart tissue is dysfunctional. It is also possible that circulating levels do not reflect cardiac levels. These are significant limitations to current biomarkers in comparison with tissue-specific cardiac biomarkers. There is a need for identification and noninvasive detection of cardiac-specific biomarkers for HF. Furthermore, Jungbauer and colleagues showed that incorporating a tandem of biomarkers, that indicate different pathological pathways, provides better prognostic indication than a single biomarker alone⁶⁰. This suggests that an approach with multiple biomarkers is useful in guiding HF management. Also, because HF is a complex syndrome with varying characteristics, a single or limited panel of biomarkers might not be reflective of its characteristics.

An emerging biomarker that is cardiac-specific and could be added to the established repertoire is the growth hormone secretagogue receptor and its ligand, ghrelin. We will further elaborate on the ghrelin/GHSR1a system in the heart as a biomarker for HF.

1.4 Ghrelin and GHSR1a

In the pursuit of discovering biomarkers for HF, there is growing interest in the hormone ghrelin and its receptor, the growth hormone secretagogue receptor (GHSR1a), and their connection to HF. There is a growing body of research supporting their use as indicators of HF.

The peptide hormone ghrelin augments systemic metabolism by stimulating appetite and regulating food intake⁶¹. Plasma ghrelin levels are elevated in a fasted state and decrease

after a meal⁶². Ghrelin is produced from cleavage of pro-ghrelin and activated after post-translational linkage to octanoic acid by ghrelin O-Acyltransferase (GOAT). The active hormone is 28 amino acids in length and its structure contains an *n*-octonoylated serine residue, the third amino acid, which is required for binding and activation of its receptor, GHSR1a. GHSR1a is a G-protein coupled receptor (GPCR) that is 366 amino acids long and contains seven transmembrane domains with an extracellular binding region for ghrelin. Its splice variant, GHSR1b, is a truncated version with 289 amino acids, and lacks transmembrane domains 6 and 7. Its biological activity is unknown^{63,64} and it does not bind ghrelin⁶⁵.

Kojima and colleagues⁶⁶ originally isolated ghrelin from rat and human stomachs, but its production has since been documented in other tissues, including the heart where it is thought to exert paracrine or autocrine functions. One of the effects of ghrelin binding and activation of GHSR1a is the release of growth hormone (GH), and some of the positive downstream effects of ghrelin on the heart are thought to be GH-dependent⁶⁷. Ghrelin has been shown to have a cardioprotective effect *in vitro* by protecting cardiomyocytes from apoptosis⁶⁸ and improves ventricular remodeling in rats following MI⁶⁹. In healthy volunteers⁷⁰ and patients with HF⁷¹, ghrelin administration reduced TPR (vasodilatory effect) and lead to an increase in CO, suggesting a potential therapeutic role in HF. Ghrelin and synthetic GHSR1a agonists like hexarelin have positive effects in cardiac remodeling in animals and humans⁷². While binding of ghrelin activates GHSR1a and results in GH release, GHSR1a mediated actions independent of GH secretion have been documented⁷³.

Notably, local cardiac production of ghrelin and myocardial expression of GHSR1a^{67,74,75} suggests that there is a ghrelin/GHSR1a system in the heart. A study conducted by Beiras-Fernandez and colleagues demonstrated that cardiac GHSR1a expression is elevated in patients with HF⁵¹. A separate study by Chen⁷⁶ et al. found that plasma ghrelin concentration is lower in patients with HF and plasma levels were related to HF severity, where high levels in the blood were related to favourable outcomes in HF patients. Ghrelin levels have also been documented to resolve to normal levels in HF patients post-heart transplantation^{78,79}.

While both ghrelin and GHSR1a have been shown to be relevant to cardiac function, ghrelin is produced by many tissues. As such, measurement of cardiac GHSR1a can be a powerful cardiac-specific biomarker for diagnosis and monitoring in HF patients.

There have been efforts to image GSHR1a using PET and SPECT. Several of these studies merely radio-labelled the ghrelin peptide to make it suitable for imaging. The first study to target GHSR1a used [¹²⁵I-*His*⁹]-Ghrelin⁸⁰. They examined its binding properties *in vitro* using samples from non-diseased human hearts and demonstrated specific and reversible binding. [¹²⁵I-*His*⁹]-Ghrelin also bound in samples of human vasculature and showed elevated uptake in atherosclerotic vessels compared to healthy vessels. However, this study was entirely *in vitro* and failed to quantify stability, clearance, and metabolism of the labelled ghrelin probe. While [¹²⁵I-*His*⁹]-Ghrelin shows promise *in vitro*, there are still questions about its *in vivo* properties and potential for use in imaging.

Kozminski and Gniazdowska⁸¹ investigated ^{99m}Tc-labeled ghrelin analogs as SPECT diagnostic imaging agents for cancer staging. Probe stability, lipophilicity, *in vitro* binding, affinity, and *in vivo* biodistribution in mice were investigated. Their results suggested that two of their compounds were stable in human serum over 120 min, but they did not show further time-points or determine a biological half-life. The same two conjugates demonstrated strong, low nanomolar binding for the receptor (54 ± 4 nM and 45 ± 3 nM). Their investigation, however, did not evaluate the probes' *in vivo* specificities or their sensitivities for detecting changes to GHSR1a expression. *In vivo* mouse studies consisted of biodistributions at 30 and 60 min post-injection with the two most promising tracers. Unfortunately, both demonstrated relatively low heart uptake (<1.5 %ID/g for both at 30 min and 60 min).

A very recent study was published that investigated possible PET and molecular imaging probes using ghrelin⁸², however these probes have yet to see *in vivo* evaluation as a potential radioligands for GHSR1a imaging. Moreover, none of the ghrelin-based probes described so far have been assessed by imaging and, while ghrelin-based tracers generally show high affinity for the receptor, they are substrates for the same metabolic enzymes as the natural hormone which impacts their *in vivo* stability and use as imaging agents.

Consequently, the ghrelin basis as structure may not be suitable for imaging⁸³. Others have developed and investigated peptidomimetic and small molecule radiolabeled tracers which may mitigate this limitation.

Labeled ghrelin and ghrelin analogs are contrasted with those of peptidomimetics in a study by Chollet and colleagues⁸³ where they assessed the potential of several ghrelin receptor agonists and inverse agonists using combinations of ghrelin and non-ghrelin mimetics. The peptides were synthesized and conjugated to the chelator NODAGA which complexes with ⁶⁸Ga. The pharmacokinetic profile and metabolic stability of the ⁶⁸Ga-NODAGA-radiotracers were investigated *in vivo* by μ PET imaging in rats. Ghrelin derived agonists accumulated in the kidneys, were not taken up by many tissues and were metabolized and cleared quickly. Their most promising candidate was an inverse agonist peptidomimetic that demonstrated stability in the blood and low blood clearance. Unfortunately, it displayed high non-specific tissue perfusion and low binding affinity. They suggested that a radionuclide with longer-half-life than ⁶⁸Ga ($t_{1/2} = 68$ min) would be useful for longer imaging studies and to better understand clearance pathways.

Potter et al.⁸⁴ investigated the ghrelin receptor as a modulator of feeding behaviour using a small molecule quinazolinone derivative and GHSR1a antagonist called (S)-6-(4-fluorophenoxy)-3-((1-[¹¹C]methylpiperidin-3-yl)methyl)-2-o-tolylquinazolin-4(3H)-one ([¹¹C]**1**). They discovered it had relatively high binding affinity *in vitro*, but it did not demonstrate high heart uptake *in vivo*, and instead distributed to the lung and liver with relatively high non-specific binding.

In light of the promise GHSR1a shows as a target in understanding the molecular mechanisms of HF, its potential use as a biomarker and therapeutic target, and the lack of encouraging imaging agents available, we sought to test a novel peptidomimetic PET tracer for noninvasive imaging of GHSR1a.

1.5 Rationale, Motivation, and Previous Work

While there are established clinical work ups to diagnose, monitor, and treat HF, clinical imaging modalities like chest radiography, echocardiography and CT largely report

changes to anatomic structure and pathologic function in the heart, which occur after HF has developed. Biomarkers can be useful in identifying subclinical changes. However, current biomarkers are produced by many tissues and are obtained from the circulation. They provide a systemic measurement of function rather than reporting solely cardiac changes. Molecular imaging of biomarkers enables researchers and clinicians to gain insight into the metabolic and molecular changes that characterize the development and progression of cardiomyopathies prior to gross structural and physiologic abnormalities. Along with the current assortment of HF biomarkers available, several others are being actively investigated. A promising candidate is GHSR1a, which binds the peptide hormone ghrelin. Human myocardial expression of GHSR as assessed by radiolabeled hexarelin was significantly higher than any other tissue evaluated⁸⁵, indicating its potential as a novel cardiac-specific biomarker for noninvasive imaging in HF.

Our group has previously synthesized and evaluated tools for visualizing GHSR1a expression. We^{86,87} and others⁸⁸ have developed fluorescent imaging agents to target GHSR1a as a biomarker of cardiomyocyte survival. The fluorescent agent is the fluorescently-tagged and truncated peptide ghrelin(1-19). Our group has since shown *in vivo* applications of modified ghrelin analogues for *in vivo* PET imaging of GHSR1a⁸⁹. We have since produced and tested the PET tracer ⁶⁸Ga-ghrelin(1-19) for targeting GHSR1a in a mouse model of diabetic cardiomyopathy, where ⁶⁸Ga-ghrelin(1-19) demonstrated correlation between receptor expression and probe uptake⁹⁰. The current lead compound is a growth hormone secretagogue (GHS), a class of low molecular weight peptidomimetics that bind GHSR1a, labelled with the longer-lived isotope ¹⁸F (half-life = 110 min) and contains unnatural amino acids in its structure which protect from degradation by peptidases *in vivo*. It has previously been characterized *in vitro* and has shown strong GHSR1a binding (IC₅₀ = 69 nm) and activation (EC₅₀ = 1.1 nm).

By moving from a fluorescent agent to a PET imaging agent, we can develop a clinically translatable probe. Using a peptidomimetic probe over the previously used ghrelin analogs should result in superior targeting, stability, and pharmacokinetics. We propose that GHSR1a may be a biomarker for subclinical cardiomyopathy and potentially provide insight into pathogenesis of the clinical syndrome of HF. In this work, we describe the *in*

in vivo characterization of our current lead compound, a GHS called [1-Nal⁴, Lys⁵(4-[¹⁸F]-FB)]G-7039, for imaging cardiac GHSR1a as a biomarker for HF.

1.6 Objectives and Hypothesis

The overall objective of our research is to image GHSR1a as a biomarker for HF. In support of our objective, this study characterizes specificity of [1-Nal⁴, Lys⁵(4-[¹⁸F]-FB)]G-7039 by PET imaging of GHSR1a *in vivo*.

1.6.1 Specific Aims

1. Evaluate specificity of [1-Nal⁴, Lys⁵(4-[¹⁸F]-FB)]G-7039 for GHSR1a *in vitro* in GHSR1a expressing cells and non-expressing cells, as well as *ex vivo* in fasted and fed normal mice to quantify probe uptake in target and non-target tissues by biodistribution.
2. Assess specificity of probe *in vivo* in wildtype (wt) and global receptor-knockout mice (*ghsr*^{-/-}). This will be evaluated with *in vivo* PET imaging of wt and *ghsr*^{-/-} mice and *ex vivo* investigations of probe biodistribution.
3. Assess the cardiac metabolic profile of fasted and fed normal mice and wt and *ghsr*^{-/-} mice using immunofluorescence microscopy of GHSR1a, GLUT4, CD36, and SERCA2a expression.
4. Quantify [1-Nal⁴, Lys⁵(4-[¹⁸F]-FB)]G-7039 specificity by relating heart SUV to GHSR1a expression in wt and *ghsr*^{-/-} mice.

1.6.1.1 General Hypothesis

We expect that [1-Nal⁴, Lys⁵(4-[¹⁸F]-FB)]G-7039 will bind GHSR1a in the heart and will be able to detect changes in GHSR1a with high specificity.

1.6.1.1.1 Specific Hypotheses

1. Ghrelin has greater affinity for GHSR1a than [1-Nal⁴, Lys⁵(4-[¹⁸F]-FB)]G-7039 and ghrelin levels are expected to be elevated in fasted mice. Therefore, [1-Nal⁴,

Lys⁵(4-[¹⁸F]-FB)]G-7039 will exhibit differential cardiac uptake, favouring fed mice.

2. *ghsr*^{-/-} mice do not express GHSR1a, so [1-Nal⁴, Lys⁵(4-[¹⁸F]-FB)]G-7039 will not be appreciably distributed to the heart and will instead show faster clearance in *ghsr*^{-/-} mice.
3. Cardiac metabolic profile of fasted mice will demonstrate preference for lipids over glucose and fasted *ghsr*^{-/-} mice will not show a preference for either lipids or glucose.
4. Heart uptake of [1-Nal⁴, Lys⁵(4-[¹⁸F]-FB)]G-7039 will be correlated to GHSR1a expression.

Chapter 2

2 Materials and Methods

2.1 Tracer Synthesis

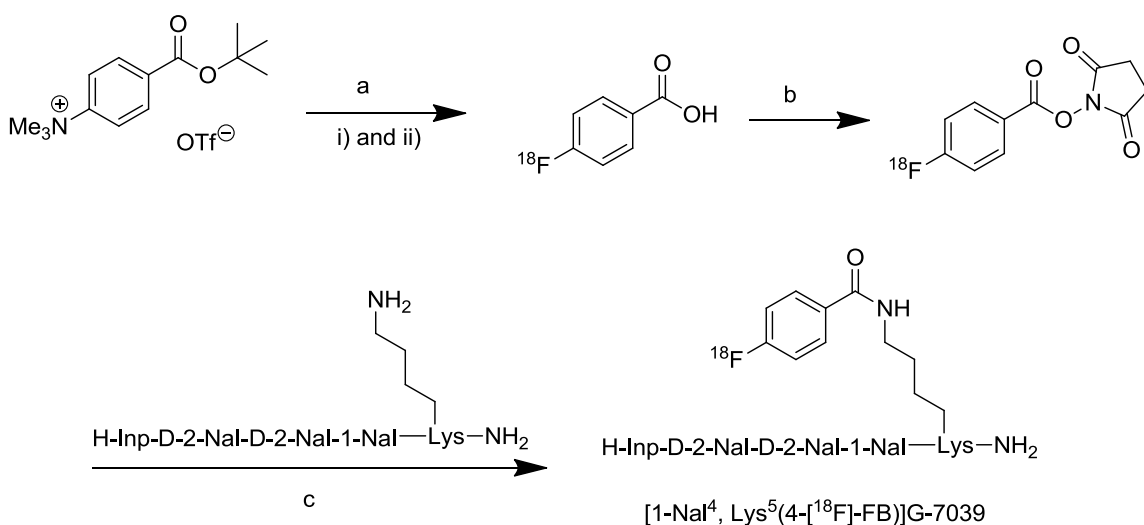
The tracer synthesis process was altered during the duration of this project, so described herein is the final method (Post-SOP), which was automated until step (b) in Scheme 1 (contrasting the initial method [Pre-SOP], which was entirely manual, and is described in Appendix A).

All the reagents and solvents used for radiosynthesis were purchased from Sigma-Aldrich unless otherwise stated. ^{18}F -fluoride was produced via the $^{18}\text{O}(\text{p},\text{n})\ ^{18}\text{F}$ reaction in a GE PETtrace 880 cyclotron at Lawson Health Research Institute for desired radiotracer synthesis. GE Tracer Lab FXN was used to prepare and purify [^{18}F]fluorobenzoic acid ([^{18}F]FBA).

As described in Scheme 1, [^{18}F]FBA was prepared on the GE tracer lab FXN. Aqueous [^{18}F]fluoride solution was trapped on the Sep-Pak AccellTM plus carbonated QMA light cartridge. 1 mL of acetonitrile/ H_2O (80/20; v/v) solution containing potassium carbonate (1 mg) and kryptofix 2.2.2 (7 mg) was used to elute [^{18}F]fluoride into the reaction vial (Scheme 1ai). The solvent was removed azeotropically in vacuum under the helium flow at 75°C. [^{18}F]fluoride was dried twice by adding 1 mL of anhydrous acetonitrile respectively under the above condition. 500 μL of anhydrous DMSO containing 5 mg of 4-(*Tert*-butoxycarbonyl)-*N,N,N*-trimethylbenzenammonium triflate salt was added into dried [^{18}F]F⁻ under helium atmosphere (Scheme 1aii). The reaction vial was sealed and heated at 120°C for 8 min. The reaction mixture was cooled down to 40°C, 1 mL of aqueous HCl (5 M) was added into reaction vial. The reaction mixture was heated 3 min at 100°C for hydrolysis of ester and then cooled down to 40°C. 2.5 mL of H_2O was added to dilute the reaction mixture. The product was trapped on Sep-Pak C18 light cartridge (Waters) and washed with 0.5 mL of H_2O . The product was eluted out by 2.5 mL anhydrous acetonitrile through drying cartridge filled with anhydrous Na_2SO_4 to get [^{18}F]FBA.

The solution of [^{18}F]FBA in 1 mL of acetonitrile was added into the vial containing 20 mg NHS (*N*-Hydroxysuccinimide) and 50 mg EDC (1-Ethyl-3-(3-dimethylaminopropyl)carbodiimide). The reaction was performed at room temperature for 8 min and then additional 50 mg of EDC was added. The solvent was removed in V-10 evaporator after additional 7 min. 1 mL of 36% Acetonitrile/ H_2O mixture was added into the reaction vial. The raw product was purified on semipreparative HPLC column. The solvent was removed on V-10 evaporator to get dried [^{18}F]SFB (radiochemical purity >99%).

The solution of 1 mg of [$^1\text{NaI}^4$]G-7039 in 500 μL acetonitrile and 100 μL H_2O was added into the above [^{18}F]SFB vial and followed by the addition of 5 μL DIPEA (*N,N*-Diisopropylethylamine) (Scheme 1c). The reaction mixture was heated at 85°C for 15 min. 500 μL H_2O was added into reaction vial after cooling down to room temperature. The reaction mixture was purified in semipreparative column to get [$^1\text{NaI}^4$, $\text{Lys}^5(4\text{-}[^{18}\text{F}\text{-FB})$]G-7039 (39% yield decay corr.).



Scheme 1. Radiosynthesis of [$^1\text{NaI}^4$, $\text{Lys}^5(4\text{-}[^{18}\text{F}\text{-FB})$]G-7039

Reagents and conditions: (a) (i) $^{18}\text{F}^-$, K_2CO_3 , Krypofix 222, DMSO, 120°C, 8 min, (ii) HCl (5 M), 100°C, 3 min; (b) NHS, EDC, acetonitrile, RT, 15 min; (c) DIPEA, acetonitrile/ H_2O , 85°C, 15 min.

2.2 *In Vitro* Characterization

Serum stability studies were performed to evaluate [1-Nal⁴, Lys⁵(4-[¹⁸F]-FB)]G-7039's biological half-life and suitable time-frames for PET imaging. For quantitative assessment of GHSR1a function, cell uptake studies were conducted by applying [1-Nal⁴, Lys⁵(4-[¹⁸F]-FB)]G-7039 to OVCAR8 cells transfected with GHSR1a and cells lacking GHSR1a at various time-points.

2.2.1 Serum Stability

[1-Nal⁴, Lys⁵(4-[¹⁸F]-FB)]G-7039 (1 mM final concentration) was incubated in a mixture of 25% human serum (Sigma-Aldrich, St. Louis, Missouri, United States; Male type AB cat# H4522) in PBS (phosphate buffered solution, pH 7.4, 450 μ L final volume, DMSO final concentration 0.5%) at 37°C. This concentration of human serum was chosen based on standard protocols observed in literature and ease of peptide extraction⁹¹. At 20, 60, 240, 420, and 1440 min after incubation, aliquots of peptide solution were removed and mixed with either acidic solution (4% phosphoric acid, pH 1-2) or basic (4% ammonium hydroxide, pH 11-13) to dissociate peptide interactions with components of human serum. Peptide was isolated from human serum by column separation on Oasis sorbent 96-well μ Elution plates (HLB- amphiphilic resin and MCX-cation exchange resin) and manifold. The extracted peptide was quantified on an Acquity UHPLC-MS system. Peptide was quantified by measuring the peak area of a peptide-specific M⁺ⁿ ion peak and averaged over 3 replicates. Percent abundance of peptide peak area relative to abundance at T₀ was plotted as a function of time. Peptide half-life was calculated by optimized curve fitting (linear, 2-parameter or 3-parameter exponential decay curve) on SigmaPlot v.12 and solving for time at 50% peptide peak abundance.

2.2.2 Cellular Uptake

Using synthesized [1-Nal⁴, Lys⁵(4-[¹⁸F]-FB)]G-7039, the *in vitro* targeting potential of the probe for GHSR1a was evaluated. OVCAR8 cells (courtesy of Dr. Trevor Shepherd, Department of Anatomy and Cell Biology, UWO, to Dr. Leonard Luyt) stably transfected with GHSR1a and non-transfected cells were released from the tissue culture flask by trypsinization and plated in a 6-well dish at a cell density of 4 x 10⁵ cells/well. The cells

were incubated overnight at 37°C and 5% CO₂ in air in RPMI (Sigma-Aldrich) containing 10% fetal bovine serum (FBS; pH 7.4). After 24 h, RPMI media with 10% FBS was removed and serum-free RPMI media was added 20 min prior to addition of tracer. [1-Nal⁴, Lys⁵(4-[¹⁸F]-FB)]G-7039 (2.8 MBq/mL) in 100% ethanol was added to each well (final ethanol concentration of ≤ 1%). After 5 min, 20 min, and 60 min incubations with 0.34–8.6 MBq of [1-Nal⁴, Lys⁵(4-[¹⁸F]-FB)]G-7039 at 37°C and 5% CO₂, cells were washed twice with PBS (pH 7.4), and detached from the plate with 0.5M EDTA (pH 8). Each time-point was repeated in triplicate in transfected and non-transfected cells.

Medium and detached cells were transferred to 0.5mL Eppendorf tubes. Radioactivity was then counted in a high-purity Ge gamma counter (Ortec GWL-190-15S, detection range 12.55-2111 keV). Activity was determined with energy windows ranging 507.18-515.43 keV and 1018.44-1026.68 keV (the energies of ¹⁸F are 511 keV and 1022 keV). The radioactivity was calculated in becquerels (Bq) and decay corrected to the time of incubation with probe. Probe uptake was calculated as a percentage relative to incubated dose (%ID).

2.3 Mice

Animal protocols were approved by the Animal Use Subcommittee at Western University (Western University, London, Ontario, Canada) and animals were treated per ethical guidelines set by the Canadian Council on Animal Care (CCAC). Documentation of ethics approval can be found in Appendix C.

For biodistribution studies, C57BL/6 mice were obtained from Charles River Laboratories (Wilmington, Massachusetts, United States) at 7-9 weeks of age and sacrificed between 8-18 weeks. *ghsr*^{-/-} mice were originally generated on a C57BL/6J background strain (generously supplied by Dr. Alfonso Abizaid, Carleton University, Ottawa, Ontario, Canada)⁹². *ghsr*^{-/-} mice were produced by breeding mice heterozygous for *ghsr*. Tail samples were obtained from offspring for genotyping when mice were 14-16 days old. Samples were genotyped by PCR using reverse and forward primers for *ghsr* and *lacZ*, which was the control for *ghsr*^{-/-} mice (Appendix D). Three female wt mice were also obtained from Jackson Laboratories (Bar Harbor, Maine, United States) at 15 weeks of age

and wt and *ghsr*^{-/-} mice were sacrificed between 16-23 weeks. All mice were fed a diet of standard rodent chow and water, and group-housed in a temperature controlled room (23°C) with a 12 h light-dark cycle with lights-on at 0700h for the study's duration.

2.4 Biodistribution

In vivo probe uptake was assessed by biodistribution in female C57BL/6 mice (8-18 weeks of age). Animals were randomly assigned to fasted or fed groups and 1 h, 2 h, or 4 h post-injection sacrifice time-points (n≥6 for each time-point in each group). Food was removed from fasted mice 4 h prior to injection and throughout biodistribution studies. Fed mice had access to food *ad libitum* throughout experiments. Both groups had access to water.

Prior to injecting the probe, animals were anaesthetized under 3% isoflurane in 100% oxygen at a constant flow rate of 2 L/min using a sealed nose cone. Once anaesthetized, mice were ventilated with a mixture of 1.5-2% isoflurane in 100% oxygen at 1.5-2 L/min constant flow rate and kept warm with a heat lamp during tail vein catheter insertion. Animals were injected with 5.23-26.4 MBq of [1-Nal⁴, Lys⁵(4-[¹⁸F]-FB)]G-7039. Post-injection, mice were recovered in normal room air and returned to their respective groups. At the appropriate time-point, mice were sacrificed by cervical dislocation under 5% isoflurane anaesthetic in 100% oxygen at 2L/min. The heart and other organs of interest were resected whole, with the exception of bone, sampled from the right tibia, and muscle, taken from the left quadriceps. Organs were weighed and their radioactivity was counted in a high-purity Ge gamma counter. The radioactivity in sampled tissues was calculated in Bq and decay corrected to the time of injection. Probe uptake was calculated as a percentage relative to the injected dose per gram of tissue (%ID/g).

2.5 μ PET and CT Imaging

In vivo probe specificity was evaluated by PET imaging of wt and *ghsr*^{-/-} mice. Animals were fasted 4 h prior to injecting the probe and then anaesthetized and ventilated as described in biodistribution studies.

2.5.1 μ PET

After insertion of a tail vein catheter, 90 min dynamic emission scans were initiated 30s before wt (n=6) and *ghsr*^{-/-} (n=6) mice were injected with 5.6-15.9 MBq of probe. Mice were scanned in an Inveon preclinical PET scanner (Siemens Medical Solutions, Erlangen, Germany), which provides a 161 mm (diameter) x 127 mm (axial) field of view, a full-width half-maximum (FWHM) between 1.4 mm and 1.8 mm, and reconstructed resolution of 1.65 mm³.⁹³ Image acquisition and reconstruction were conducted using scanner supplied software (Inveon Acquisition Workspace and microQ Viewer, respectively).

Once PET scanning concluded, the mouse and bed were removed together and transported to the CT scanner, taking care to maintain the mouse's position on the bed and the same anaesthetic conditions during the transfer. These precautions ensured minimal movement of the mouse between PET and CT scans.

2.5.2 Computed Tomography

Computed Tomography (CT) scans were acquired on a clinical Revolution CT scanner (General Electric, Schenectady New York, United States). Mice were anaesthetized as in the dynamic PET scan. The CT acquisitions were performed with settings of 4.0 cm FOV, 120 kV, 300 mA, and 192 slices of 0.625 mm thickness. Total scan time was 1.0 s. Scans provided anatomical reference for PET scans.

Following CT scans, mice were sacrificed and biodistributions were performed as described in Section (2.4). Time of sacrifice post-injection varied with several factors including transport from PET to CT machines. Mice were sacrificed between 2-2.5 h after injection with the probe.

2.5.3 PET Image Reconstruction and Analysis

Dynamic PET imaging data was binned into 13 imaging frames of 12 frames x 5 min and 1 frame x 30 min (2.5x zoom and Nyquist filter applied). Data was decay corrected to the time of injection and images were corrected for dead time, random and scatter coincidences prior to reconstruction using the three iterations of ordered subsets-expectation maximization algorithm (OSEM3D; 18 iterations of 16 subsets) with scanner supplied

software (microQ viewer) and analysis in 3D Slicer (v. 4.6.2). Standardized uptake values were calculated using Equation 1 below from volumes of interest (VOIs) drawn around volumes corresponding to the heart, lungs, and abdomen on PET images overlaid with CT images. Heart uptake was corrected for spillover activity from the lungs using Equation 2, where RC is the recovery coefficient (which we have set equal to 0.93 for the mouse heart, based on values for a phantom of similar size⁹⁴).

Equation 1. SUV calculation

$$SUV = \text{activity concentration in VOI [Bq/cc]} \times \frac{\text{mouse body weight [g]}}{\text{total activity injected [Bq]}}$$

Equation 2. Heart SUV correction

$$SUV_{\text{Heart Corrected}} = \frac{SUV_{\text{Heart}} - (1 - RC) \times SUV_{\text{Lung}}}{RC}$$

2.6 ELISA

During biodistribution and proceeding imaging studies, 75 μL of whole blood was collected into heparinized syringes by cardiac puncture. Samples were dispensed into tubes containing 25 μL Complete, Mini protease inhibitors (Sigma-Aldrich) in PBS, gently mixed, and stored and transported on ice. Tubes were centrifuged at 3000 rpm for 10 min at 4°C, then 50 μL aliquots of supernatant plasma were collected and stored at -80°C until assayed.

Plasma samples were thawed at room temperature, 40 μL was collected, and ELISA was conducted (LUMINEX 200 multiplex assay, Luminex Corporation, Austin, Texas, United States). Blood plasma samples were analyzed for concentrations of ghrelin, glucagon, glucagon-like peptide-1 (GLP-1), and insulin and results were given in pg/mL.

2.7 Immunofluorescence Microscopy of Heart and Lungs

Immunofluorescence microscopy was used to evaluate expression of GHSR1a in the heart and lungs, as well as to assess markers of metabolism and contractility in heart samples.

2.7.1 Hearts

After counting radioactivity, excised hearts from fasted and fed mice sacrificed at 1 h post-injection and wt and *ghsr*^{-/-} mice were fixed in 4% paraformaldehyde (PFA; Electron Microscopy Sciences, Hatfield, Pennsylvania, United States) buffered with PBS (pH 7.0-7.4). Hearts were then perfused in increasingly higher concentrations of sucrose solution (5%, 10%, 15%, each for at least 30 min, then 30% for 24 h), dried, and embedded in frozen tissue embedding medium (OCT; ThermoFisher Scientific, Waltham, Massachusetts, United States) and then frozen at -80°C. Serial sections were cut (Leica CM 1850 cryostat) at 7µm thickness and four sections were selected for immunohistochemistry per subject. Tissue sections were thawed in PBS and incubated in blocking buffer (1% Bovine Serum Albumin [BSA] and 10% donkey or goat serum in PBS) for 30 min at room temperature. Serial sections were stained with primary polyclonal antibodies as described in Table 2 for 1 h at room temperature. GHSR1a was stained for using a fluorescent Cy5-ghrelin probe (1:100) we have previously characterized in murine cardiac tissue⁸⁶. Secondary donkey anti-goat antibodies conjugated to fluorophore Alexa Fluor 488 (1:500, Life Technologies, Carlsbad, California, United States) and secondary donkey anti-rabbit antibody conjugated to fluorophore Alexa Fluor 594 (1:500, Invitrogen, Carlsbad, California, United States) for visualization of ghrelin, SERCA2a, CD36, and GLUT4 were applied for 2 h at room temperature. Primary and secondary Antibodies and Cy5-ghrelin were diluted in blocking buffer. Coverslips were then mounted with ProLong Gold liquid mountant containing DAPI nuclear stain (ThermoFisher Scientific, Waltham, Massachusetts, United States). Tissue sections were stored overnight at 4°C and coverslips were sealed the next day.

Table 2. Primary antibodies used for immunofluorescence microscopy.

Antigen	Catalog #	Dilution	Host	RRID#	Source Company
Ghrelin	sc-10368	1:100	Goat	AB_2232479	Santa Cruz Biotechnology
Serca2A	ab3625	1:300	Rabbit	AB_303961	Abcam
CD36	nb400-144	1:200	Rabbit	AB_10003498	Novus Biologicals
GLUT4	sc-1608	1:100	Goat	AB_445037	Santa Cruz Biotechnology

2.7.2 Lungs

Three wt and three *ghsr*^{-/-} mice (29 weeks of age) were selected for microscopy to quantify GHSR expression in pulmonary tissue. Mice were sacrificed with an intraperitoneal injection of sodium pentobarbital (110mg/mL, Lundbeck, Valby, Denmark). A midline incision was made in the abdomen and through the diaphragm and ribcage. The vena cava was injected with 50µL of heparin (1000IU/mL) and a cannula was inserted and secured in the right pulmonary artery. The vasculature was infused with 1mL saline through a small incision in the left ventricle. The lungs, heart, and trachea were removed intact. Lungs were suspended and filled with 4% PFA fixative to a pressure of 15 cm H₂O. An airtight knot was drawn around the trachea and lungs were immersed in 4% PFA for 24 h⁹⁵. Lungs were resuspended in PBS post-fixation, changing solution every 12 h for 48h. Finally, the lungs were immersed in 70% ethanol and stored at 4°C until further processing.

Lungs were placed coronally in cassettes for paraffin embedding. Lungs were embedded in paraffin wax and sectioned sequentially from anterior to posterior. Three sections per subject were selected for H&E staining approximately 14 µm apart and three adjacent sections were stained for GHSR1a with Cy5-ghrelin.

2.7.3 Microscopy Image Acquisition and Quantification

Five random fields of view per cardiac and pulmonary tissue section were acquired at 20x magnification (for immunofluorescence microscopy: Nikon NIS Elements v. BR 4.50.00, Shinagawa, Tokyo, Japan; and for histology: Northern Eclipse v5.15.4.0, EMPIX Imaging, Mississauga, Ontario, Canada). GHSR1a was imaged with a Cy5 filter with 100ms exposure. Ghrelin and GLUT4 were imaged with FITC filter with 800ms exposure. CD36 and SERCA2a were imaged with TRITC filter with 500ms exposure.

Images were imported for analysis into FIJI v. 1.49v, a distribution of ImageJ (National Institutes of Health, Bethesda, Maryland, United States). Fluorescence was quantified using a custom FIJI script that measures fluorescent intensity, which represents protein levels, across an image and returns the raw integrated density, as done previously^{86,96}.

2.8 Statistical Analyses

Statistical analyses were conducted and graphs were plotted using GraphPad Prism v. 7.00 (San Diego, California, United States). Differences in cell uptake were analyzed using two-way repeated measures ANOVA and Bonferroni post-hoc test. For biodistributions, within group differences between organs sampled and between time-points in fasted, fed, wt, and *ghsr*^{-/-} mice were determined using two-way ANOVA followed by Tukey's multiple comparisons test. Between group differences in fasted and fed mice in matching organs at the same time-point were analyzed by two-way ANOVA and Bonferroni's multiple comparisons test. Two-way ANOVA was also used to assess differences in plasma proteins evaluated by ELISA. Data from dynamic PET SUVs was evaluated using two-way repeated measures ANOVA followed by Bonferroni's multiple comparison's test for between group differences and Tukey's multiple comparison's test for within groups differences. Static PET SUVs and between group comparisons of plasma protein levels from ELISA measurements were evaluated using unpaired two-tailed Student's t-test. For immunofluorescence microscopy images, differences in mean fluorescence between fasted and fed mice and between wt and *ghsr*^{-/-} mice were determined by two-way ANOVA and Bonferroni's multiple comparisons test. Grubb's test was used to address outliers in plasma

protein and fluorescence data. Outliers were removed from final analysis. For correlations, linear regression analysis was used. Significance was set at $p < 0.05$ for all statistical tests.

2.9 Acknowledgements

Technical assistance for studies was generously provided by many individuals. Genotyping was performed by Vivarium Services at Victoria Research Laboratories (London Health Sciences Center). ELISA was conducted by Shannon Seney (Lawson Health Research Institute). Lungs were excised and fixed with generous assistance from Lynda McCaig (Department of Physiology and Pharmacology, UWO) and prepared for embedding with help from Karen Nygard (Biotron, UWO). Embedding, sectioning, and staining were performed by Caroline O'Neil (Robarts' Molecular Pathology Laboratory). Support in heart sectioning, staining and imaging came from Derek Wu (Pathology and Laboratory Medicine, UWO). Probe synthesis, cell uptake, and serum stability studies were conducted and assisted by Tyler Lalonde and Lihai Yu (Department of Chemistry, UWO).

Chapter 3

3 Results

3.1 Physicochemical Characteristics of [1-Nal⁴, Lys⁵(4-[¹⁸F]-FB)]G-7039

Note: [1-Nal⁴, Lys⁵(4-[¹⁸F]-FB)]G-7039 was synthesized, radiolabeled, and HPLC analyzed pre-SOP by Tyler Lalonde (Appendix A) and post-SOP by Lihai Yu (described below).

The chemical structure of [1-Nal⁴, Lys⁵(4-[¹⁸F]-FB)]G-7039 is shown in Figure 1. Receptor binding assays in human embryonic kidney (HEK293) cells stably transfected with GHSR1a were previously conducted to assess the binding affinity of [1-Nal⁴, Lys⁵(4-[¹⁸F]-FB)]G-7039⁹⁷. The binding affinity was evaluated by the half-maximal inhibitory concentration and was found to be IC₅₀ = 69 nM. Calcium flux assays were used to determine the receptor activation as determined by the half-maximal effective concentration (EC₅₀), which was calculated as EC₅₀ = 1.1 nM. The same properties were assessed in human ghrelin and determined to be IC₅₀ = 7.63 nM and EC₅₀ = 1.6 nM⁹⁷. The partition coefficient (log*P*) was calculated using ACD/Log*P* software to assess [1-Nal⁴, Lys⁵(4-[¹⁸F]-FB)]G-7039 lipophilicity and was found to be 8.76 ± 0.88.

Using the Post-SOP synthesis method yielded [1-Nal⁴, Lys⁵(4-[¹⁸F]-FB)]G-7039 with a decay-corrected radiochemical yield of 39%, radiochemical purity ≥ 99% and a molar activity of > 4.7 GBq/μmol after 81 min.

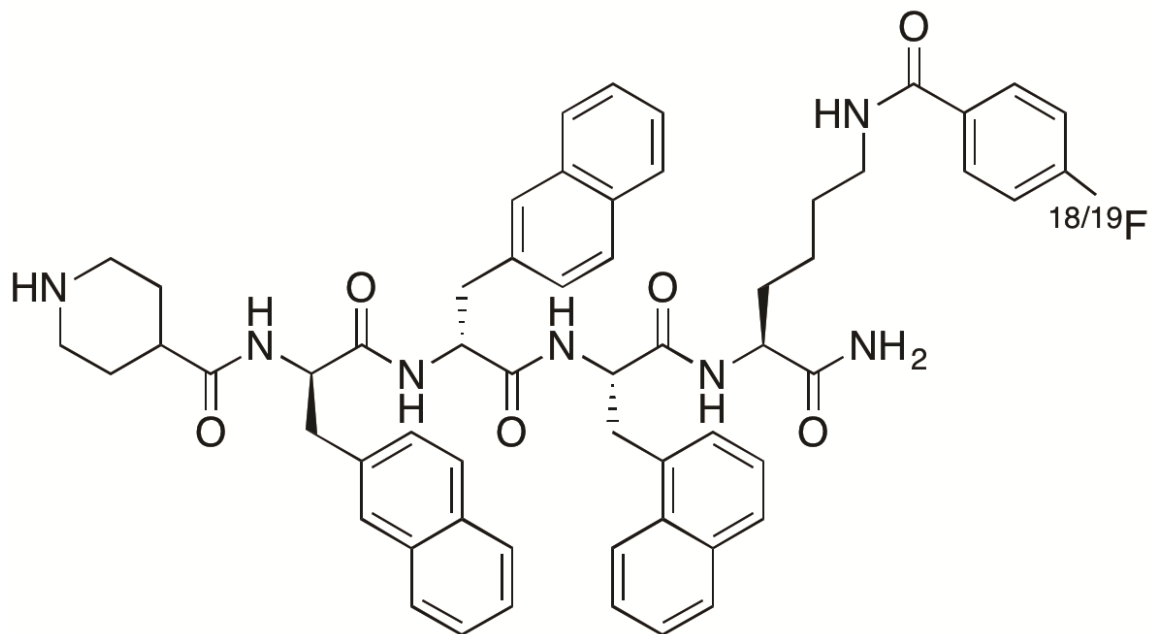


Figure 1. Chemical structure of [1-Nal⁴, Lys⁵(4-[¹⁸F]-FB)]G-7039

[1-Nal⁴, Lys⁵(4-[¹⁸F]-FB)]G-7039's *in vitro* binding affinity is $IC_{50} = 69$ nM and its *in vitro* potency is $EC_{50} = 1.1$ nM. The partition coefficient was calculated as $\log P = 8.76 \pm 0.88$.

3.1.1 Serum Stability of Unlabeled Probe

Serum stability was analyzed in 25% human serum in PBS at 37°C to determine the *in vitro* stability of the unlabeled compound [1-Nal⁴, Lys⁵(4-FB)]G-7039. Peptide half-life was calculated by optimized curve fitting. An exponential decay curve was generated (Figure 2) and described by Equation 3 below, where “y” represents the percentage of remaining peptide and “t” represents the time in minutes.

Equation 3. [1-Nal⁴, Lys⁵(4-FB)]G-7039 biological decay

$$y = 99.8e^{-0.0009t} - 1.7$$

Based on Equation 3, the half-life of [1-Nal⁴, Lys⁵(4-FB)]G-7039 in 25% human serum is 730.8 min (12.2 h). By extrapolation, the physical half-life in 100% serum would be 182.7 min (3.05 h).

3.1.2 Cellular Uptake of [1-Nal⁴, Lys⁵(4-[¹⁸F]-FB)]G-7039

Uptake of [1-Nal⁴, Lys⁵(4-[¹⁸F]-FB)]G-7039 in OVCAR8 cells stably transfected with GHSR1a was compared to wt cells lacking the receptor. Two-way repeated measures analysis of variance determined that there were differences with respect to time point ($p < 0.01$) and cell type ($p < 0.05$). As shown in Figure 3, both groups demonstrated a time-dependent uptake pattern. Bonferroni post-hoc analysis did not return differences between wt and transfected cells at any of the time-points examined.

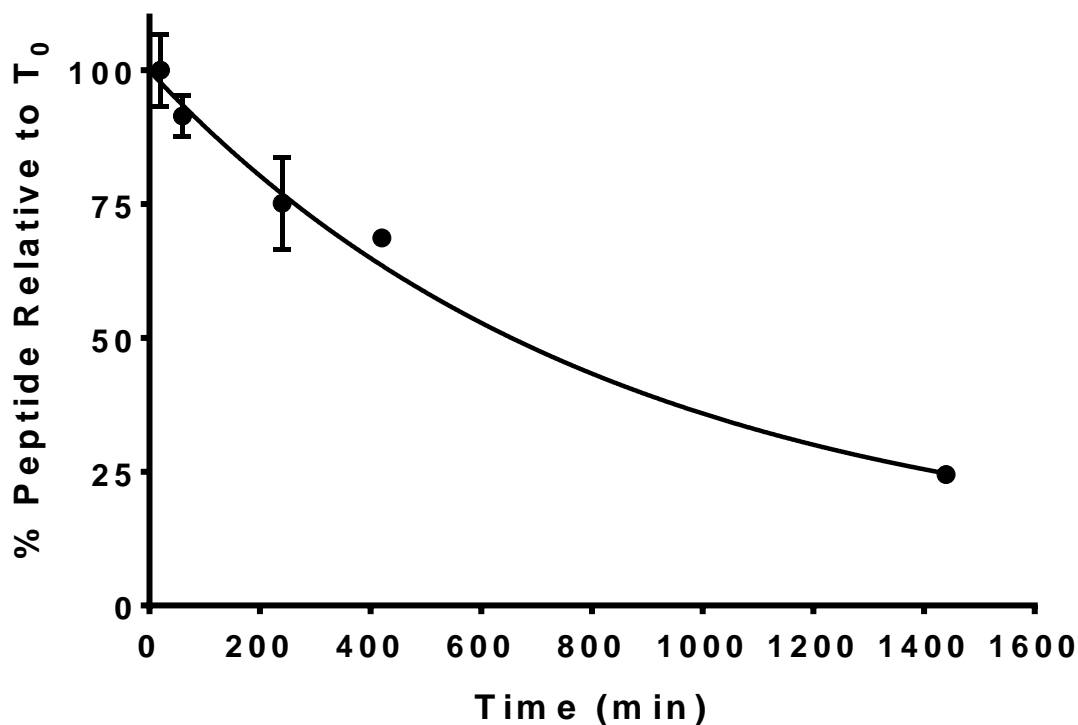


Figure 2. *In Vitro* serum stability of [1-Nal⁴, Lys⁵(4-FB)]G-7039

Stability of [1-Nal⁴, Lys⁵(4-FB)]G-7039 was assessed *in vitro* by incubating 1 mM of peptide in human serum at 20, 60, 240, 420, and 1440 min. Data points represent the average of three replicates \pm SEM and are presented as a percentage of peptide abundance relative to abundance at T₀.

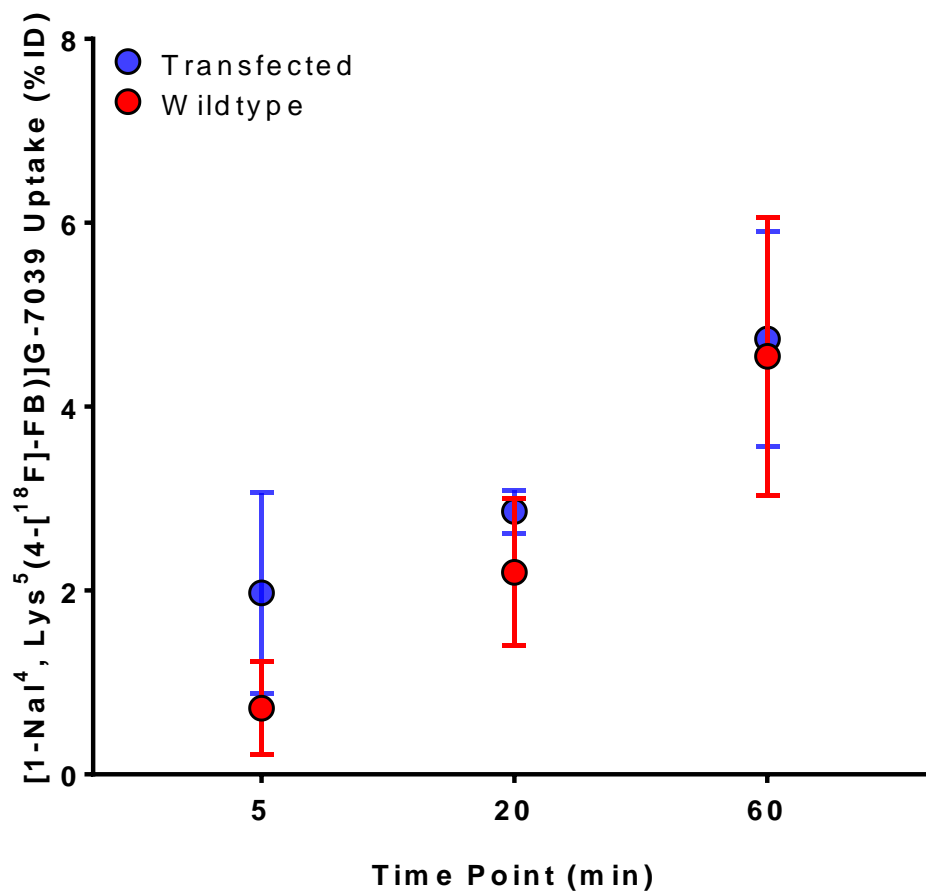


Figure 3. Cell uptake of [1-Nal⁴, Lys⁵(4-[¹⁸F]-FB)]G-7039

The target cell uptake of [1-Nal⁴, Lys⁵(4-[¹⁸F]-FB)]G-7039 in OVCAR8 cells stably transfected with GHSR1a (blue) and wt OVCAR8 cells (red). Uptake was time-dependent in both cell types with no differences in uptake between them. Each value is presented as mean \pm SEM (n=3).

3.2 *Ex Vivo* Biodistribution in Fasted and Fed Mice

Ex vivo biodistributions were conducted in fasted and fed female C57BL/6 mice to determine the time-point and conditions where uptake of [1-Nal⁴, Lys⁵(4-[¹⁸F]-FB)]G-7039 was highest in the heart, thus providing support for a suitable imaging protocol (Figures 4 & 16). Uptake values were calculated as a percentage of the decay corrected total injected dose and normalized to each tissue's weight (%ID/g). Because the first step in the synthesis protocol for [1-Nal⁴, Lys⁵(4-[¹⁸F]-FB)]G-7039 was changed from manual to automated (pre-/post-SOP), we evaluated biodistributions using both methods. The Post-SOP results are shown below. Pre-SOP results can be found in Appendix B.

3.2.1 Results Post-SOP

[1-Nal⁴, Lys⁵(4-[¹⁸F]-FB)]G-7039 exhibited similar uptake profiles in fasted and fed mice (Figure 4). Negligible heart uptake was observed in both groups. The probe distributed primarily to the lung, spleen, liver, and urine. Differences between fed and fasted mice at the same time-point were not significant except in urine at 2 h ($p < 0.05$). Within groups, differences in uptake were observed between time-points in the same organ and between organs at the same time-point.

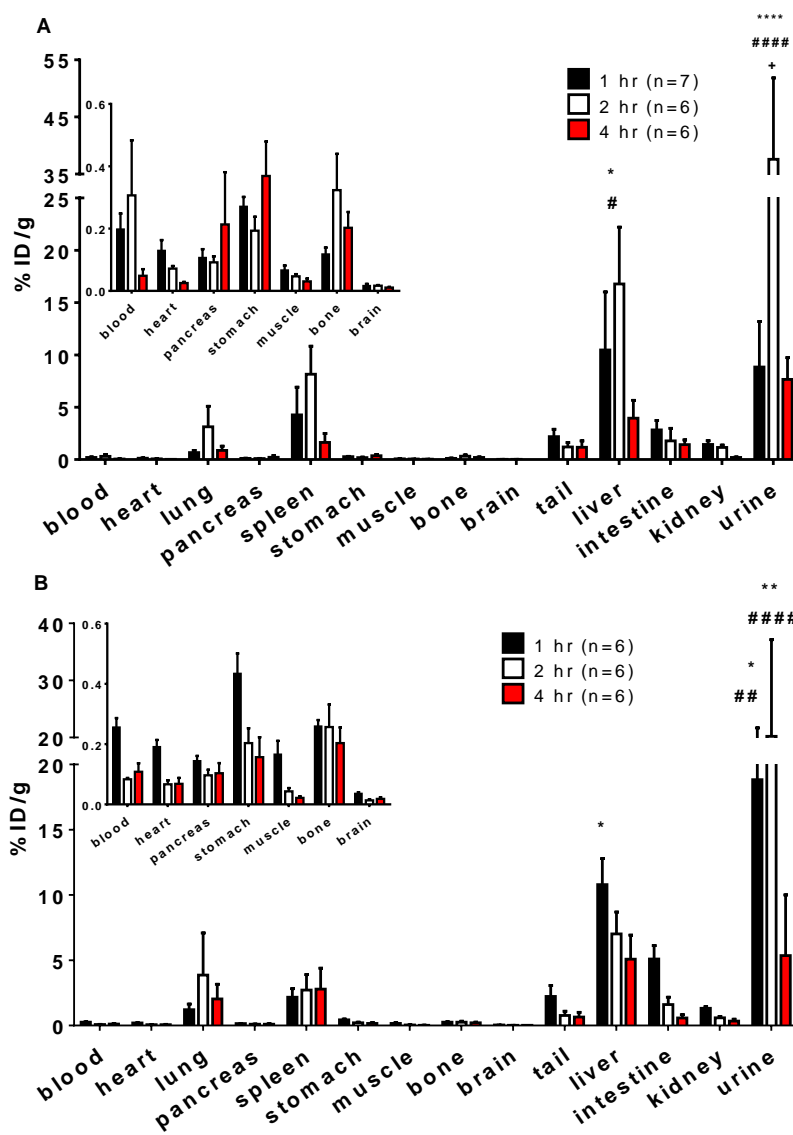


Figure 4. Biodistribution profile of [1-Nal₄, Lys₅(4-[¹⁸F]-FB)]G-7039 using Post-SOP probe synthesis

Fasted (**A**) and fed (**B**) female C57BL/6 mice injected with [1-Nal₄, Lys₅(4-[¹⁸F]-FB)]G-7039 were sacrificed 1 h, 2 h, and 4 h post-injection. Urine samples are n=4, 6, 5 in (**A**) and n=2, 4, 5 in (**B**) at 1 h, 2 h, and 4 h respectively. Values are mean injected dose per gram tissue (%ID/g) ± SEM. As shown in (**A**): **p*<0.05 in liver at 2 h vs all tissues (except spleen), *****p*<0.0001 in urine at 2 h vs all other tissues, #*p*<0.05 in liver at 2 h vs 4 h, #####*p*<0.0001 in urine at 1 h vs 2 h and 2 h vs 4 h, and +*p*<0.05 in fasted urine vs fed urine. As shown in (**B**): **p*<0.05 in liver at 1 h vs all tissues (except spleen, tail, and urine), and in urine at 1 h vs all tissues (except liver), ***p*<0.01 in urine at 2 h vs all tissues, and ##*p*<0.01 in urine at 1 h vs 4 h and ####*p*<0.0001 at 2 h vs 4 h.

3.3 Plasma Concentrations of Ghrelin, Glucagon, GLP-1, and Insulin in Fasted and Fed Mice

To establish whether circulating ghrelin affected binding, plasma levels of ghrelin, along with other proteins known to be influenced by nutritional state (glucagon, glucagon-like peptide-1 [GLP-1], and insulin) were assessed by ELISA using blood samples from fasted and fed mice sacrificed 1 h, 2 h, and 4 h post-injection (Figure 5). Concentrations are given in pg/mL. Plasma ghrelin levels were independent of time point or nutritional state as evaluated by analysis of variance. No differences between fasted and fed were observed in other time-point-matched plasma protein concentrations.

3.4 Heart Immunofluorescence in Fasted and Fed Mice

Sections of hearts excised from fasted (n=8) and fed (n=6) mice sacrificed 1 h post-injection were imaged using immunofluorescence microscopy to evaluate expression of cardiac GHSR1a and markers of cardiac contractility and metabolism, ghrelin, GLUT4, SERCA2a, and CD36. Two-way analysis of variance returned significant differences with respect to marker and nutritional state. As shown in Figure 6, post-hoc Bonferroni analysis revealed significantly lower cardiac ghrelin ($p<0.05$) levels and cardiac GLUT4 ($p<0.01$) expression in fasted mice compared to fed mice. There were no differences observed in the other markers.

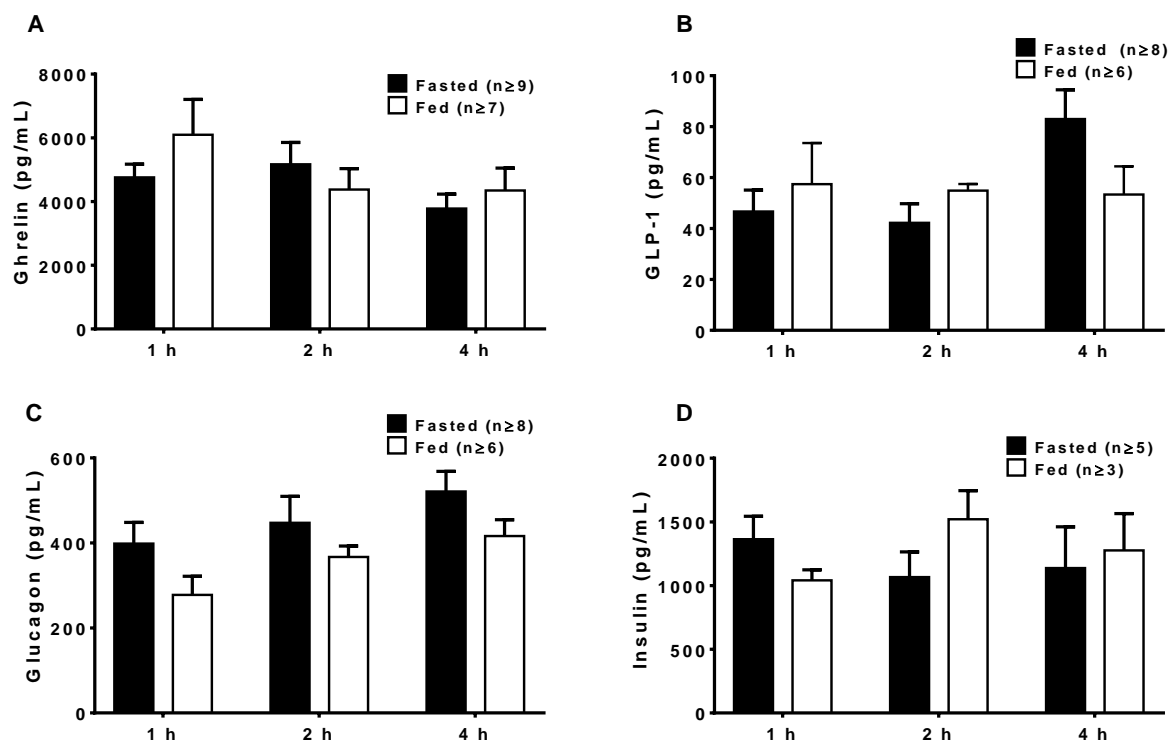


Figure 5. Plasma concentration of ghrelin, GLP-1, glucagon, and insulin in fasted and fed mice

Blood plasma concentrations of (A) ghrelin, (B) glucagon-like peptide-1 (GLP-1), (C) glucagon, and (D) insulin in fasted and fed mice sacrificed 1 h, 2 h, and 4 h post-injection of [1-Nal⁴, Lys⁵(4-[¹⁸F]-FB)]G-7039. Values are shown as mean concentration in pg/mL ± SEM.

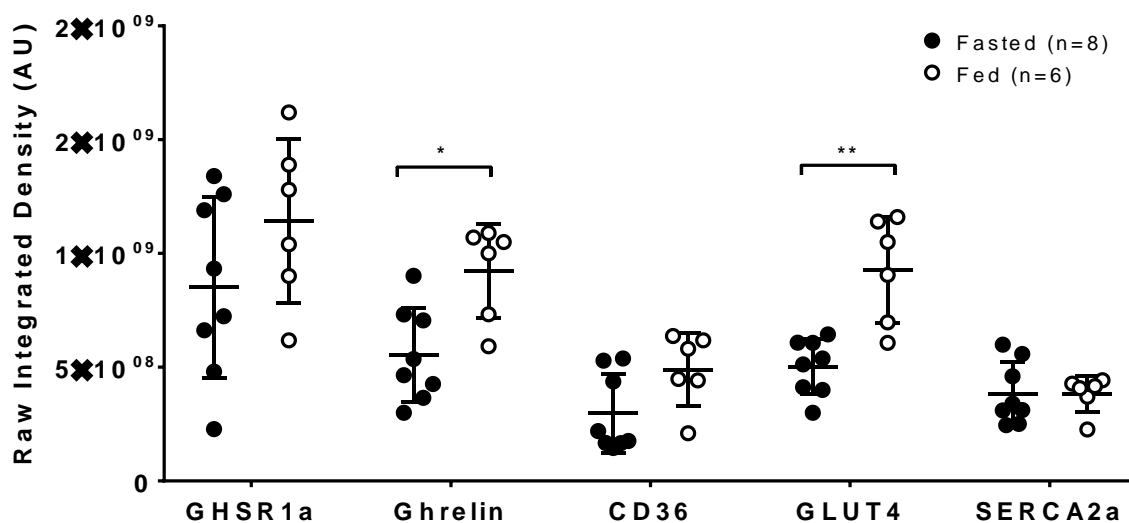


Figure 6. Metabolic profiles of heart samples from fasted and fed mice

Cardiac protein levels of metabolic markers (represented by fluorescent intensity) between fasted (n=8) and fed (n=6) mice sacrificed 1 h post-injection as assessed by immunofluorescence microscopy. Values are given in raw integrated density (arbitrary units) of fluorescence. The middle line represents the mean value and the bars indicate SEM. * $p < 0.05$, ** $p < 0.01$.

3.5 *In Vivo* μ PET-CT Imaging

To validate [1-Nal⁴, Lys⁵(4-[¹⁸F]-FB)]G-7039 specificity for GHSR1a *in vivo*, wildtype C57BL/6J and global receptor knockout (*ghsr*^{-/-}) mice were imaged in list-mode for 60 min followed by a 30 min static scan. PET images indicated that the regions with greatest signal intensity corresponded to the lungs and abdomen (Figure 7), but images revealed no appreciable signal in the heart, aside from the 5 min frame. The signal appeared to decrease in the lungs in a time dependent manner as it increased in the abdomen.

3.5.1 Time-Activity Curves in wt and *ghsr*^{-/-} Mice

SUVs were calculated from VOIs assigned to the heart and regions with greatest signal, corresponding to the lungs and abdomen. Heart uptake as assessed by dynamic (Figure 9) and static (Figure 10) PET was not different between wt and *ghsr*^{-/-} mice. Of note, static SUVs in the heart were significantly correlated ($p < 0.0001$, $r = 0.91$) with lung SUVs (Figure 8), indicating that VOIs drawn around the heart were detecting signal from the lungs. Heart SUVs were corrected for lung spillover using Equation 2 and results are shown alongside original heart SUVs in Figures 9 and 10. After spillover correction, heart SUVs were no longer correlated to lung SUVs ($r = 0.46$).

Analysis of variance determined that differences in mouse model were not significant in all VOIs investigated for dynamic imaging. Within group differences were found in all VOIs for time dependent distribution with earlier time points having greatest uptake in heart and lung and later time points having greater uptake in the abdomen as indicated in Figure 9.

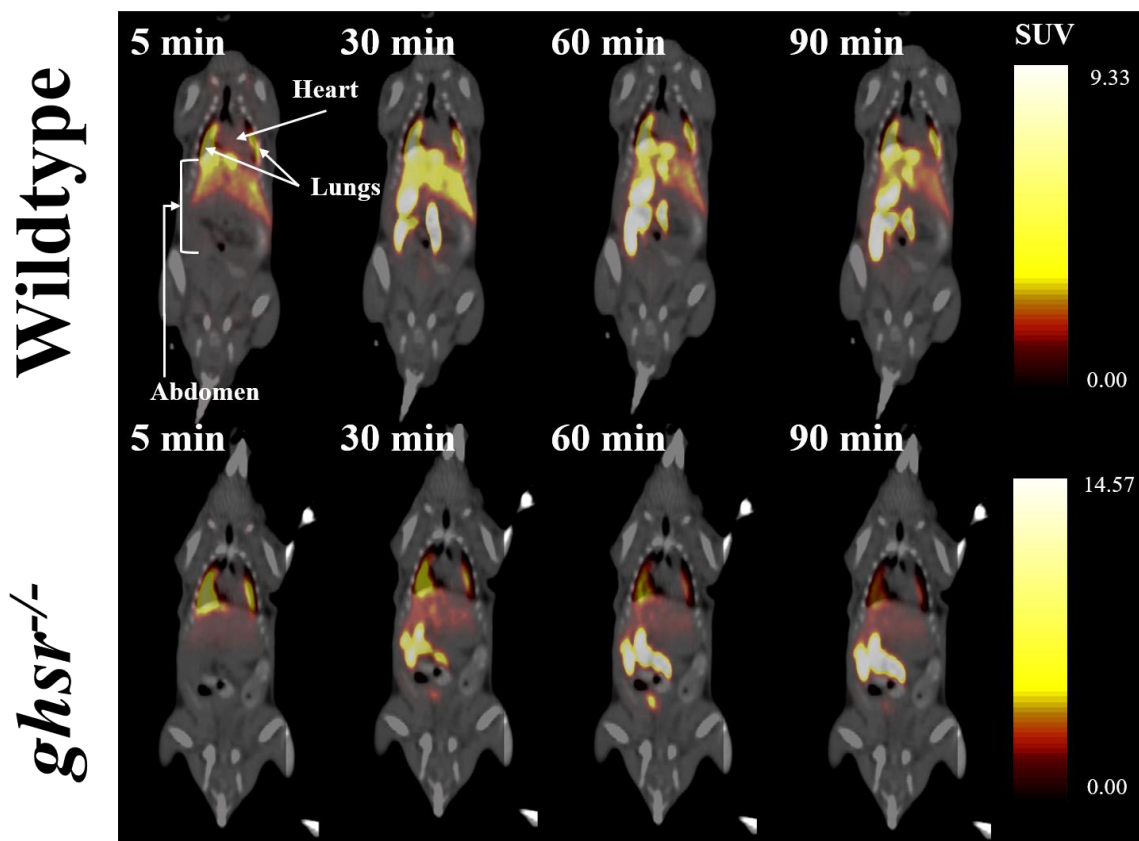


Figure 7. μ PET-CT imaging in wt and *ghsr*^{-/-} mice

Distribution pattern of [1-NaI⁴, Lys⁵(4-[¹⁸F]-FB)]G-7039 in wt (top) and *ghsr*^{-/-} (bottom) mice recorded with PET. All frames shown are integrated over a 5 min time period, except the 90 min frame which was integrated over 30 min. Coronal slices through the mouse body at the section of liver are shown with view from anterior. The arrows indicated regions where VOIs were drawn.

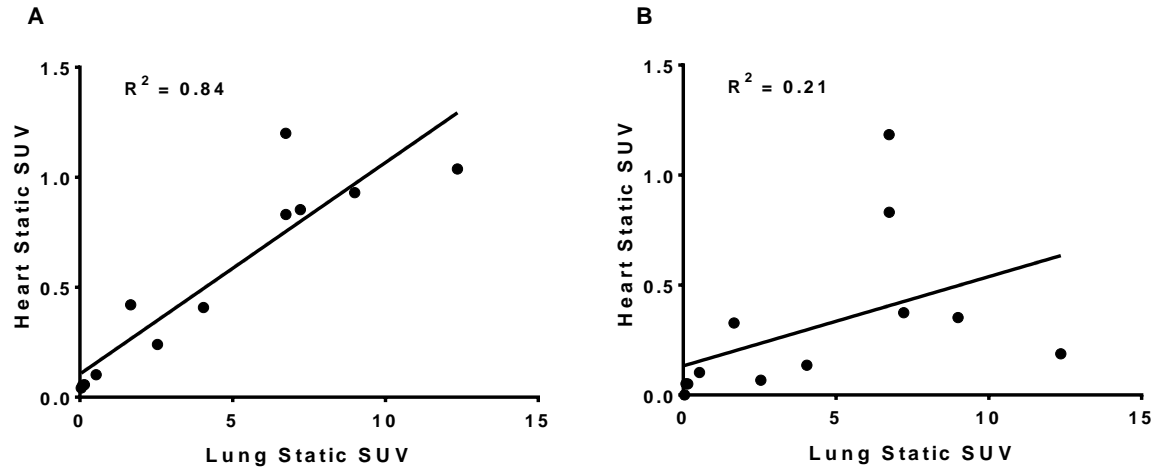


Figure 8. Heart SUV pattern is similar to lung SUVs

Correlation between static SUVs in the lung and static SUVs in the heart before spillover correction (**A**) shows a strong positive trend. The slope of the line is significantly non-zero ($p < 0.0001$). After spillover correction (**B**), there is no correlation.

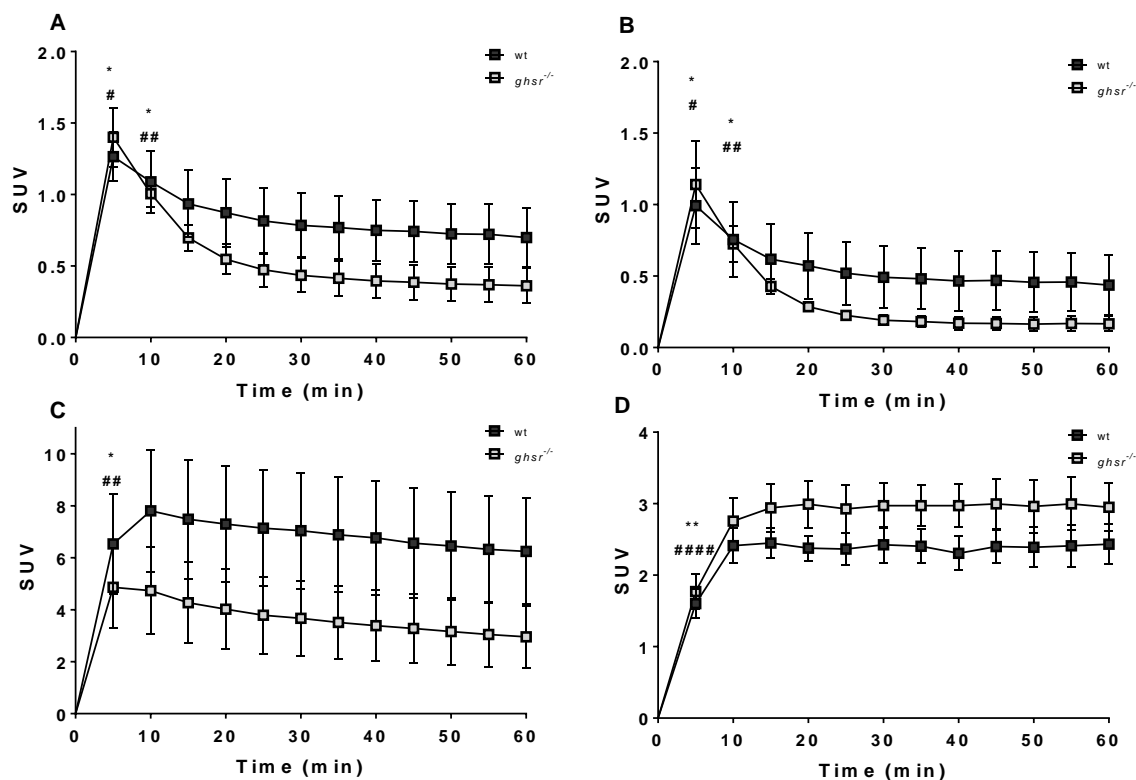


Figure 9. Time-activity curves for [1-Nal⁴, Lys⁵(4-[¹⁸F]-FB)]G-7039 uptake in wt and *ghsr*^{-/-} mice

Heart (A), spill-over corrected heart (B), lung (C), and abdomen (D) uptake of [1-Nal⁴, Lys⁵(4-[¹⁸F]-FB)]G-7039. TACs are expressed as SUVs and values are means \pm SEM (n=6 for wt and n=6 for *ghsr*^{-/-}). *in wt and #in KO. As shown in (A) and (B): * p <0.05 and ## p <0.05 at 5 min and 10 min vs all time-points (except 15 min). As shown in (C): * p <0.05 and ### p <0.01 at 5 min vs all time-points. As shown in (D): ** p <0.01 and ##### p <0.0001 at 5 min vs all time-points.

3.5.2 Static PET in wt and *ghsr*^{-/-} Mice

To determine if [1-Nal⁴, Lys⁵(4-[¹⁸F]-FB)]G-7039 PET could detect changes in GHSR1a expression, static images were acquired over 30 min, at 1 h after probe injection in both wt (n=6) and *ghsr*^{-/-} (n=6) mice. The heart was not visualized (Figure 7, 90 min). Probe uptake was mainly in the lungs and abdomen. The SUVs (mean ± SEM) calculated in the heart (0.69 ± 0.20 vs 0.34 ± 0.12 in wt vs *ghsr*^{-/-}, respectively; corrected: 0.44 ± 0.19 vs 0.17 ± 0.06), lungs (5.90 ± 1.96 vs 2.62 ± 1.10), and abdomen (2.44 ± 0.29 vs 2.93 ± 0.31) were not significantly different between groups in any VOI.

3.5.3 *Ex Vivo* Biodistributions in wt and *ghsr*^{-/-} Mice

Following imaging studies, wt (n=3) and *ghsr*^{-/-} (n=3) mice were euthanized and biodistribution was performed (Figure 11). Again, negligible heart uptake was observed and uptake of [1-Nal⁴, Lys⁵(4-[¹⁸F]-FB)]G-7039 was highest in the lungs of wt mice ($p < 0.0001$) compared to *ghsr*^{-/-} mice. In wt mice, the lung also had the highest uptake compared to all other tissues ($p < 0.0001$).

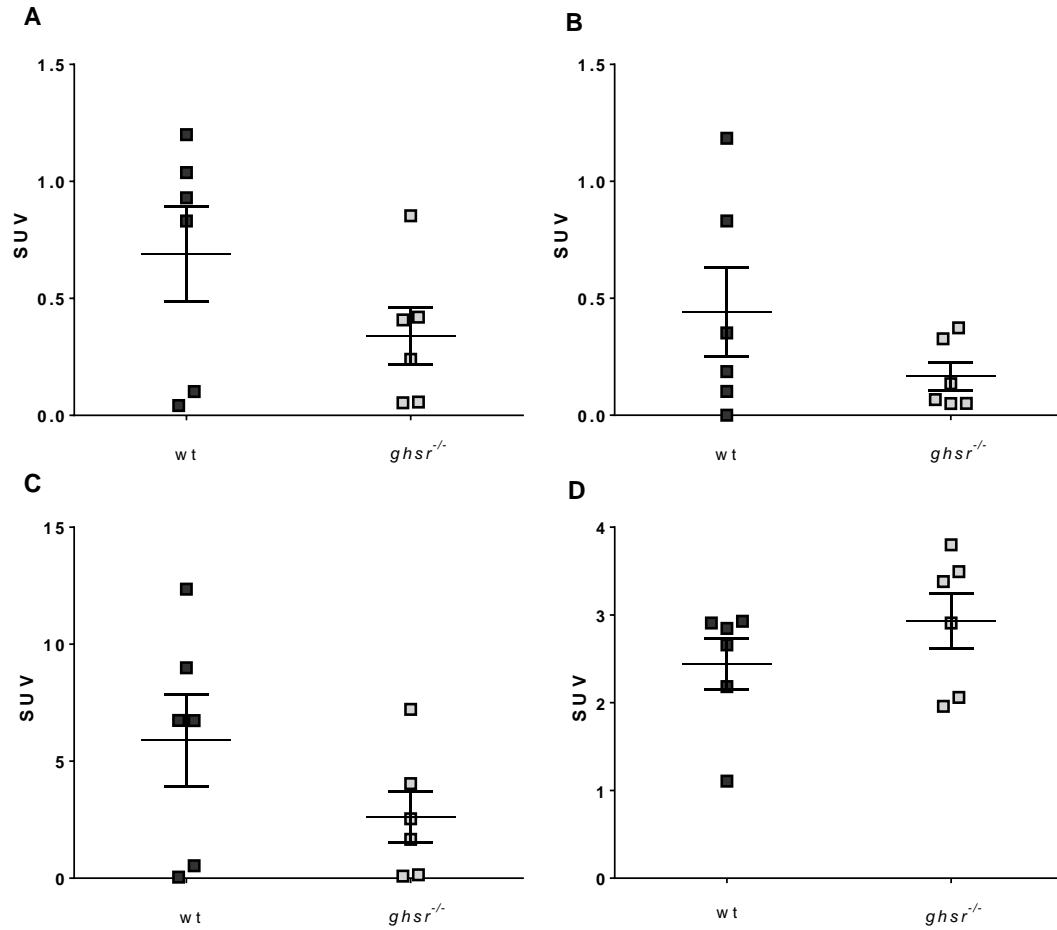


Figure 10. Static SUVs in wt and *ghsr*^{-/-} mice

Heart (A), spill-over corrected heart (B), lung (C) and abdomen (D) 60 min post-injection and over a 30 min time frame. No differences between wt and *ghsr*^{-/-} were observed in any VOIs.

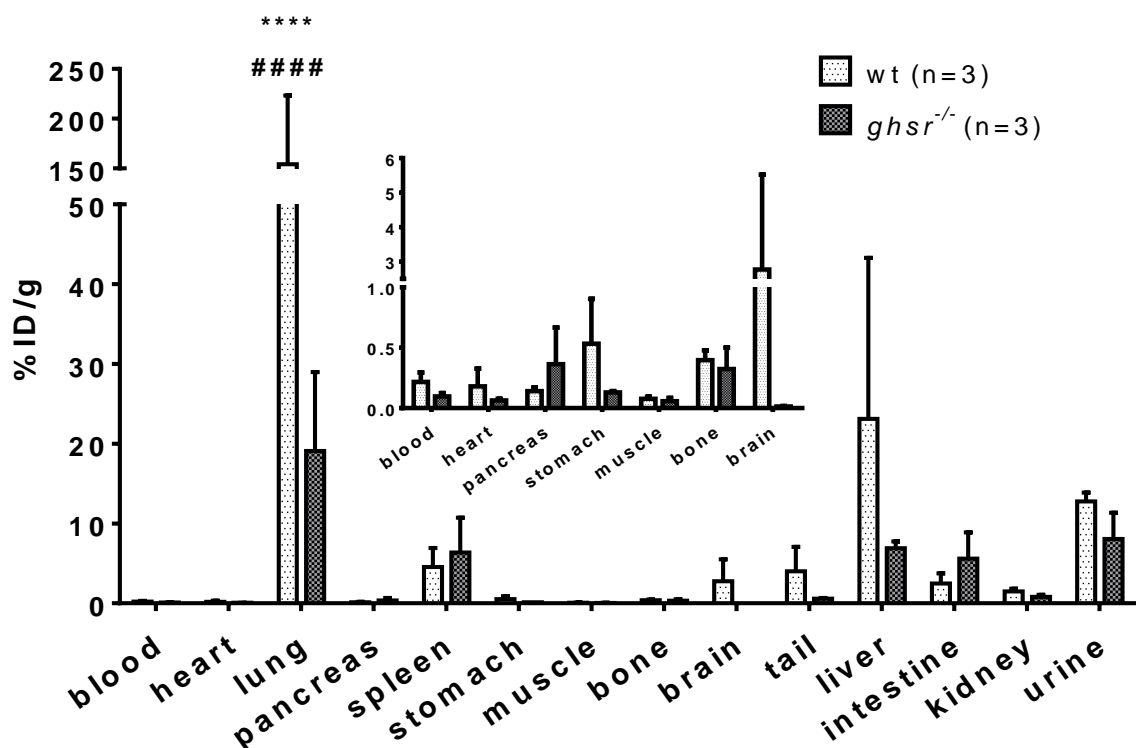


Figure 11. Biodistribution in wt and *ghsr*^{-/-} mice

Biodistributions conducted on wt and *ghsr*^{-/-} following PET-CT imaging (2-2.5 h post-injection). Values are mean %ID/g \pm SEM for each group. **** p <0.0001 in lung vs all tissues (except liver) and ##### p <0.0001 in wt compared to *ghsr*^{-/-}.

3.5.4 Heart Immunofluorescence in wt and *ghsr*^{-/-} Mice

As in fasted and fed mice, hearts from wt (n=6) and *ghsr*^{-/-} (n=6) mice sacrificed proceeding PET-CT imaging studies were embedded, sectioned, and stained for GHSR1a, ghrelin, GLUT4, SERCA2a, and CD36, and imaged using immunofluorescence microscopy. GHSR1a expression was significantly less in *ghsr*^{-/-} mice ($p < 0.001$). Differences were not observed between wt and *ghsr*^{-/-} mice in any other markers stained for (Figure 12). Notably, some GHSR1a fluorescence was detected in the hearts from *ghsr*^{-/-} mice.

Cardiac ghrelin expression and corrected heart SUVs were plotted as a function of cardiac GHSR1a expression to assess relationship between cardiac ghrelin and its receptor as well as probe sensitivity for differential GHSR1a expression (Figure 13). To relate systemic and cardiac ghrelin levels, plasma ghrelin concentration was plotted against cardiac ghrelin and the relationship between heart SUV and circulating ghrelin was plotted (Figure 13C and 13D). No convincing correlations were observed between cardiac ghrelin expression and cardiac GHSR1a expression ($r = 0.43$), heart SUV and GHSR1a expression ($r = 0.47$) or plasma ghrelin ($r = -0.16$), or plasma and cardiac ghrelin ($r = -0.23$).

3.6 Lung Immunofluorescence in wt and *ghsr*^{-/-} Mice

Imaging and biodistribution studies revealed significant [1-Nal⁴, Lys⁵(4-[¹⁸F]-FB)]G-7039 uptake in the lungs, so we sought to evaluate GHSR1a expression and qualitatively visualize receptor distribution in lung tissue. Lungs from wt (n=3) and *ghsr*^{-/-} (n=3) mice were stained to visualize nuclei by H&E and for GHSR1a expression on adjacent sections. Fluorescence imaging showed expression of GHSR1a in the lungs of both groups (Figure 14A), but no differences in GHSR1a levels were found (Figure 14B).

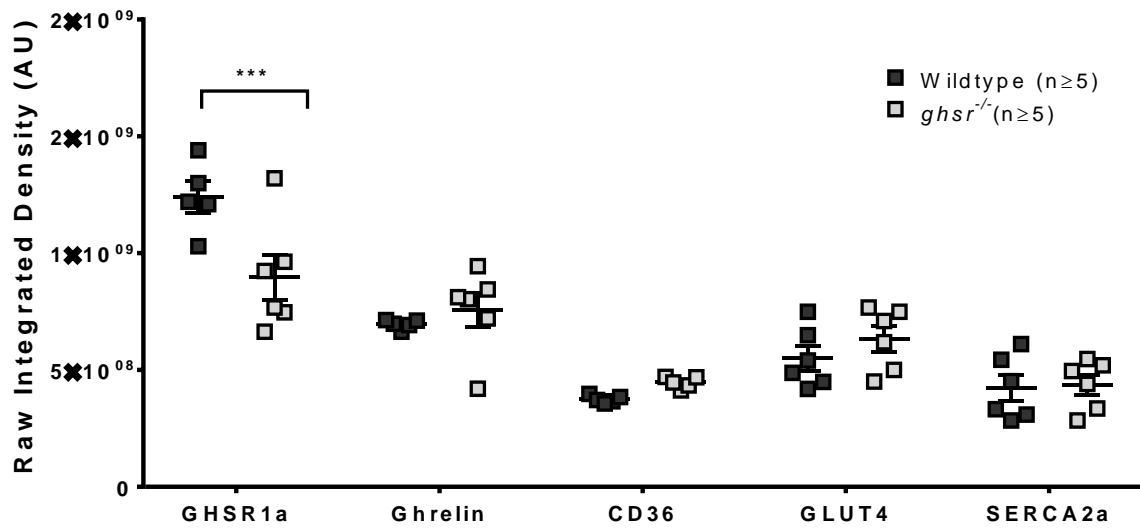


Figure 12. Metabolic profiles of heart samples from wt and *ghsr*^{-/-} mice

Cardiac protein levels of metabolic markers (represented by fluorescent intensity) between wt (n≥5) and *ghsr*^{-/-} (n≥5) mice sacrificed post-PET-CT imaging as assessed by immunofluorescence microscopy. Values are given in raw integrated density (arbitrary units) of fluorescence. The middle line represents the mean value and the error bars indicate SEM. * $p < 0.001$.

3.6.1.1 GHSR1a Expression and Plasma Ghrelin Concentrations Compared to Heart SUV

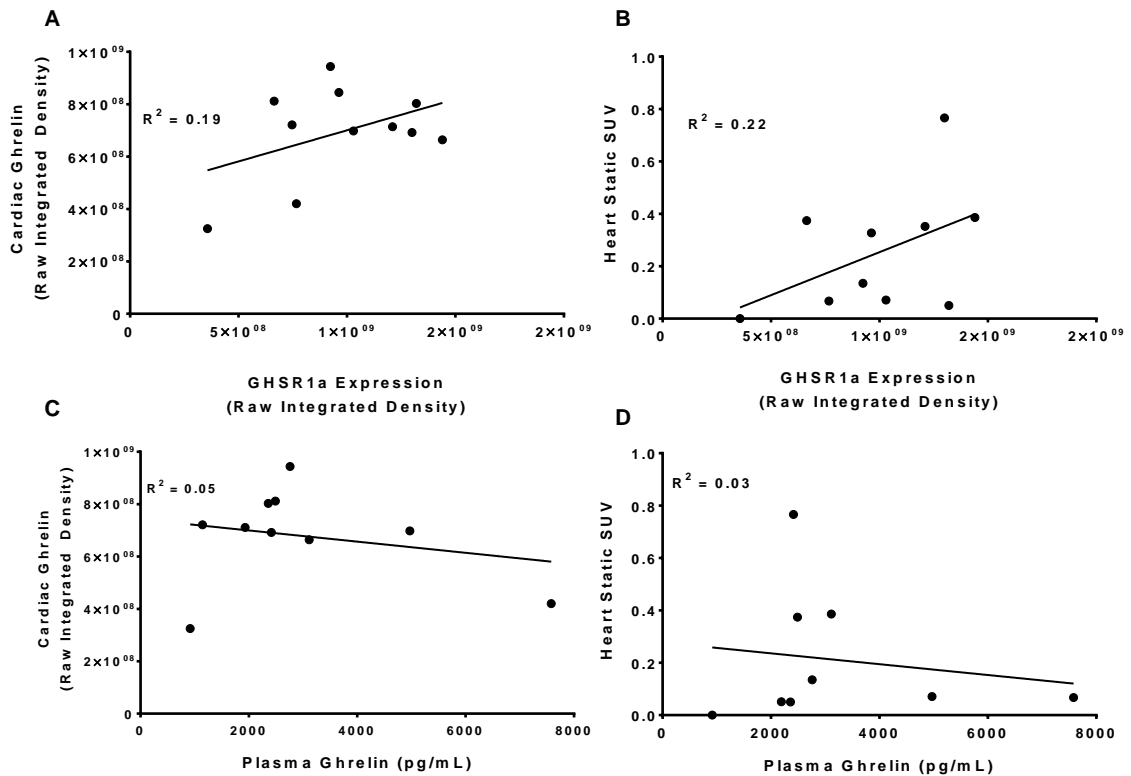


Figure 13. Correlations of cardiac ghrelin expression, heart SUV, and plasma ghrelin with cardiac GHSR1a expression

Cardiac ghrelin expression (A) and static SUVs from VOIs assigned to heart in wt (n=5) and *ghsr*^{-/-} (n=6) mice (B) plotted as a function of GHSR1a expression. (C) plasma ghrelin concentration as a function of cardiac ghrelin expression and (D) heart SUV correlation with plasma ghrelin. Each point represents a value from a single mouse.

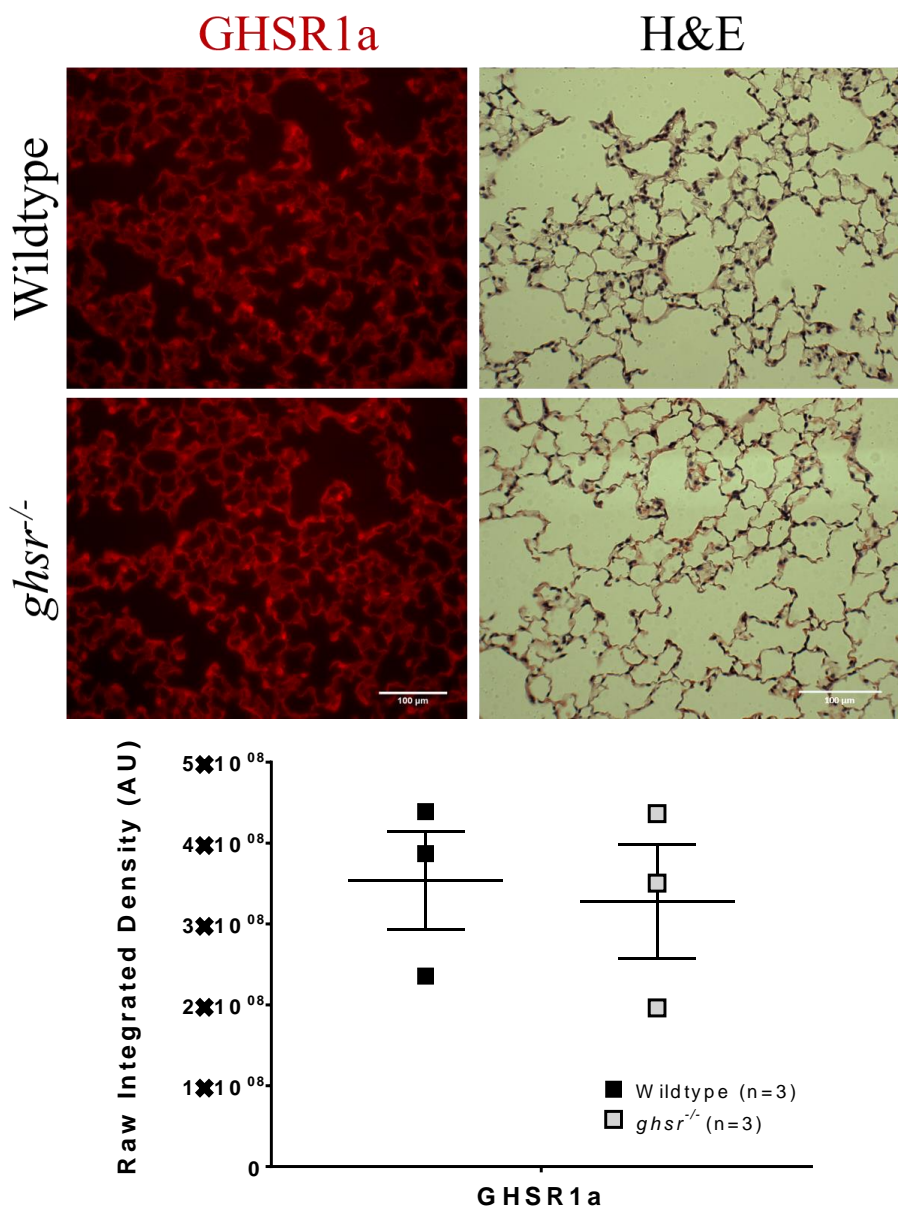


Figure 14. Lung expression of GHSR1a in wt and *ghsr*^{-/-} mice

(A) Representative fluorescent (left panels) and light microscope (right panels) images of alveolar cells show the distribution of GHSR1a (red). Nuclei in adjacent 7 μm sections are highlighted with H&E stain. (B) pulmonary expression of GHSR1a (represented by fluorescent intensity) in wt (n=3) and *ghsr*^{-/-} (n=3) mice as assessed by immunofluorescence microscopy. Values are given in raw integrated density (arbitrary units) of fluorescence. The middle line represents the mean value and the error bars indicate SEM.

Chapter 4

4 Discussion

HF is a progressive disease and a major cause of morbidity and mortality in patients suffering from it. It is resource intensive and requires significant economic investment. Investigations into understanding the fundamental biochemical pathways underlying HF etiology and progression have resulted in development of targeted pharmacologic and surgical interventions, in the hopes of mitigating the effects of HF. Laboratory tests are helpful in identifying signs of end-stage organ dysfunction secondary to the late stages of HF in the liver or kidneys by examining electrolyte imbalances or neurohormonal activation. However, these tests measure circulating biomarkers that are not localized to the heart and are expressed by other tissues. As well, current clinical imaging is useful for defining heart size, shape, and function to some extent, but most clinical imaging targets gross changes to structure and function which occur late in the development of HF. Of the available clinical imaging modalities, PET can elucidate biochemical information regarding development and evolution of pathology. This study characterized a PET tracer designed to target a biomarker endogenous to heart tissue.

The expression of cardiac GHSR1a is elevated in patients with HF, so we characterized the peptidomimetic GHSR1a ligand [1-Nal⁴, Lys⁵(4-[¹⁸F]-FB)]G-7039 for PET imaging of cardiac GHSR1a. We hypothesized that [1-Nal⁴, Lys⁵(4-[¹⁸F]-FB)]G-7039 would bind GHSR1a with high specificity. Briefly, the objectives of this study were to 1) evaluate [1-Nal⁴, Lys⁵(4-[¹⁸F]-FB)]G-7039 binding specificity and distribution *in vitro* and in healthy mice, 2) establish [1-Nal⁴, Lys⁵(4-[¹⁸F]-FB)]G-7039 specificity for GHSR1a *in vivo* using wt and *ghsr*^{-/-} mice, 3) establish a metabolic profile in the hearts of fasted and fed C57BL/6 mice and wt and *ghsr*^{-/-} mice, and 4) quantify specificity by relating cardiac receptor expression and [1-Nal⁴, Lys⁵(4-[¹⁸F]-FB)]G-7039 uptake.

4.1 Physicochemical properties of [1-Nal⁴, Lys⁵(4-[¹⁸F]-FB)]G-7039

The *in vitro* binding, activation, and hydrophobicity of [1-Nal⁴, Lys⁵(4-[¹⁸F]-FB)]G-7039 have been previously evaluated⁹⁷. [1-Nal⁴, Lys⁵(4-[¹⁸F]-FB)]G-7039 displayed nanomolar

binding affinity ($IC_{50} = 69$ nM) in previous work using HEK293/ghrelin receptor cells, which was within an order of magnitude of native human ghrelin ($IC_{50} = 7.63$ nM). It also had strong *in vitro* potency ($EC_{50} = 1.1$ nM), demonstrating that it is a potent ghrelin receptor agonist, whereas endogenous human ghrelin is also a strong agonist ($EC_{50} = 1.6$ nM). This is important for obtaining signal from the target tissue as GHSR1a is internalized in response to agonist binding to protect from overstimulation. The ability to internalize with the receptor is reasoned to make radiolabeled agonists better for persistent signal and accumulating in tissues of interest, thus improving contrast and *in vivo* visualization. An agonist tracer was useful for this work because receptor-ligand internalization is less likely for antagonists. GHSR1a antagonists have been characterized as imaging agents, but demonstrated non-specific uptake and retention only in clearance tissues⁸⁴. However, the properties of antagonists and inverse agonists allow their use for mapping of receptor expression⁹⁸.

At the outset of this study, we experienced difficulties with consistent tracer synthesis, variable yield, and low molar activity. In an effort to address these problems, the method for [1-Nal⁴, Lys⁵(4-[¹⁸F]-FB)]G-7039 generation was altered so that the first step in synthesis was automated. Using the Post-SOP method, radiochemical purity marginally improved from >98% to >99%. Decay corrected yield was nearly equivalent, but more consistent (29-63% Pre-SOP, averaging 52%, to 39% Post SOP). Importantly, there were dramatic improvements to synthesis time (from 140 min to 81 min), thus improving the amount of initial activity for studies, and molar activity (116 MBq/ μ mol to > 4.7 GBq/ μ mol).

The partition coefficient ($\log P$) is a measure of a compound's hydrophobicity (by comparing its distribution in octanol and water). Favourable values for drugs and imaging agents are in the range of 1-3⁹⁹. A higher $\log P$ often results in non-specific binding and, if the $\log P$ value is too high, the imaging agent's solubility is severely reduced and the probe is quickly eliminated *in vivo*¹⁰⁰. Therefore, an appropriate $\log P$ value is crucial for *in vivo* imaging. [1-Nal⁴, Lys⁵(4-[¹⁸F]-FB)]G-7039 has a $\log P$ of 8.76 ± 0.88 suggesting a challenge for *in vivo* imaging. However, others have noted that the $\log P$ is not necessarily a predictor of *in vivo* behavior¹⁰¹ and it is not always easy to predict non-specific binding

*in vivo*²⁶. Moreover, [1-Nal⁴, Lys⁵(4-[¹⁸F]-FB)]G-7039 was the lead compound developed by our group to target GHSR1a, exhibiting promising binding properties and potency compared to the next leading compound⁹⁷, so further *in vitro* and *in vivo* characterization of [1-Nal⁴, Lys⁵(4-[¹⁸F]-FB)]G-7039 was performed.

4.2 Stability and Cellular Uptake

The biological half-life of [1-Nal⁴, Lys⁵(4-FB)]G-7039 was tested in human serum to assess its stability and help in establishing a time-frame for imaging. Its physical half-life is 3.05 h. Imaging experiments and biodistributions at 1 h and 2 h were well within one half-life, and 4 h biodistributions were within two half-lives. Native ghrelin has been reported to have an *in vitro* half-life of 4 h in human serum and 30 min in rat serum¹⁰². Others have reported an *in vivo* half-life of less than 1 h¹⁰³ and 10 min⁷⁰. The greater biological half-life observed for [1-Nal⁴, Lys⁵(4-FB)]G-7039 compared to ghrelin may be explained by the presence of unnatural and D-amino acids its sequence that protect it from degradation by peptidases *in vivo*. Moreover, some ghrelin analog tracers exhibit biological half-lives of less than 5 min⁸³, while others are stable at 120 min⁸¹. Thus, [1-Nal⁴, Lys⁵(4-FB)]G-7039 is a relatively stable compound. Notably, *in vitro* serum stability was tested, which does not account for metabolism in the liver and other tissues.

The specificity of [1-Nal⁴, Lys⁵(4-FB)]G-7039 was examined by cellular uptake in both GHSR1a-expressing OVCAR8 cells and in wildtype cells not expressing the receptor. The probe had a similar uptake pattern in both groups of cells, where uptake was time-dependent and independent of receptor expression. This could be due to non-specific binding and internalization due to the probe's highly lipophilic character allowing it to cross plasma membranes, unlike ghrelin which does not freely cross cell membranes¹⁰⁴. It should be noted that the lipophilic character of the probe made administration especially difficult so relatively high quantities were added to cells and this may have contributed to cell uptake by saturation kinetics.

In vitro cell uptake studies have the advantage of comparing uptake with respect to ability to accumulate in cells purely as a function of receptor presence and *in vitro* stability in stationary serum can assess metabolism directly related to circulating components. In

contrast to *in vitro* studies, *in vivo* studies can account for many other factors that affect PET probe uptake, including biodistribution across tissues, metabolism in peripheral organs and whole blood, and elimination. *In vivo* studies provide information on tissue accumulation and time to elimination. Differences in probe behaviour between *in vitro* and *in vivo* are common²⁶, so it is prudent to also evaluate in animal models to obtain a more complete pharmacologic profile. *In vivo* target specificity for GHSR1a was evaluated by conducting biodistribution studies in female C57BL/6 mice.

4.3 Probe Specificity and Effects of Nutritional State on Binding

Specific aim (1) was intended to address [1-Nal⁴, Lys⁵(4-[¹⁸F]-FB)]G-7039 specificity *in vivo*. This was investigated by conducting *ex vivo* biodistributions in female C57BL/6 mice. Our group has previously documented higher expression of GHSR1a in the C57BL/6 mouse heart compared to several other tissues⁸⁷, so this was an appropriate model for imaging cardiac GHSR1a.

Ghrelin has a higher binding affinity for GHSR1a than [1-Nal⁴, Lys⁵(4-[¹⁸F]-FB)]G-7039⁹⁷, and its secretion is predominantly dictated by nutritional state such that circulating ghrelin levels are greater when fasted compared to when fed⁶². In order to ascertain the best conditions for imaging, we sought to evaluate if fasting affected probe binding *in vivo* and to determine the optimal time-point post-injection for imaging.

The biodistribution profile of [1-Nal⁴, Lys⁵(4-[¹⁸F]-FB)]G-7039 using the Post-SOP synthesis method was similar in both fasted and fed mice. Primarily, minimal heart uptake was observed in both groups at all time-points. Instead, the tissues that displayed high uptake were the lungs, spleen, tail, liver, intestines, and kidneys. High activity was observed in the urine, even within the first hour, indicating fast clearance. Lipophilic tracers are commonly transported through the circulation by binding plasma proteins⁸³; however, fast clearance may explain why tracer distribution to the blood was low. The high activity in the kidneys and liver indicates sites of excretion and metabolism, respectively.

Using the Pre-SOP synthesis method, blood concentration of [1-Nal⁴, Lys⁵(4-[¹⁸F]-FB)]G-7039 was stable over time. [1-Nal⁴, Lys⁵(4-[¹⁸F]-FB)]G-7039 distributed to the heart, and its uptake appeared to stay consistently elevated across the time-points examined. Human studies investigating GHSR expression in various tissues found GHSR1b mRNA is highly expressed (greater than GHSR1a) in the myocardium, but it is unlikely that [1-Nal⁴, Lys⁵(4-[¹⁸F]-FB)]G-7039 is binding GHSR1b because GHSR1b does not bind or respond to ghrelin or GHS⁶³. Uptake at 1 h was noticeably higher for nearly all tissues, indicating that the probe is being eliminated. Non-specific perfusion in all tissues with a slow blood clearance even after 1 h suggests the probe is being bound by plasma proteins⁸³. Aside from uptake in the first hour, liver uptake increased with time from 4 h to 6 h and steadily washed out of kidneys, lungs, and spleen. This suggests hepatobiliary metabolism and excretion as the primary clearance pathway.

The presence of impurities can explain divergent biodistribution using the two synthesis methods. The final product is the same in both cases, so its stability remains unchanged, however lower bone uptake using the Post-SOP synthesis (<1% compared to ~1-1.5%) supports the idea that reactants like [¹⁸F]FBA and [¹⁸F]SFB may have been present in the final product. Furthermore, lower molar activity using the Pre-SOP method indicates the presence of unlabeled product, which likely exhibits the same distribution pattern as the final product using the Post-SOP method, thereby displacing [1-Nal⁴, Lys⁵(4-[¹⁸F]-FB)]G-7039 by binding the same sites without returning measurable signal. Interestingly, using the Post-SOP synthesis method, the probe did not show high uptake in the brain, which is known to express high amounts of GHSR1a¹⁰⁵. Even though [1-Nal⁴, Lys⁵(4-[¹⁸F]-FB)]G-7039 is lipophilic, it is likely that the concentration gradient from blood to brain was too low to facilitate transport in the case of Post-SOP synthesis. Meanwhile, brain uptake was reasonably elevated using the Pre-SOP synthesis method where the concentration gradient was likely high enough to facilitate crossing of the blood brain barrier.

Biodistribution in fasted mice using Pre-SOP synthesis (Appendix B) demonstrated highest heart uptake of [1-Nal⁴, Lys⁵(4-[¹⁸F]-FB)]G-7039 in mice sacrificed 1 h and 4 h post-injection. Considering *in vitro* half-life was less than 4 h, and only one animal was sampled

for fed uptake using Pre-SOP methods prior to changeover to Post-SOP, fasting mice prior to imaging and imaging within the first hour after probe injection appeared appropriate.

4.4 Circulating Metabolic Hormones

After a 4 h fast, there were no differences in plasma concentrations of ghrelin, GLP-1, glucagon, and insulin, which were selected because their circulating concentrations are dependent of nutritional state. Such a brief fast may not have been long enough to induce measurable metabolic changes. Others have found that fasting for 24 h resulted in elevated plasma ghrelin levels in C57BL/6 mice¹⁰⁶, so this may be a more appropriate fasting time-period. Also, fed mice had access to food *ad libitum* so there may have been differences in feeding behaviour in individual mice which potentially lead to variations in ghrelin levels among fed mice. Distribution of [1-Nal⁴, Lys⁵(4-[¹⁸F]-FB)]G-7039 in the heart may be unaffected by circulating ghrelin, however no relationship could be discerned because there were no differences in cardiac probe uptake or plasma ghrelin between fasted and fed mice.

4.5 Time-Activity Curves

Focal uptake was not visualized in the heart after injection of probe, aside from the 5 min frame, which can be explained as a first-pass effect. Heart and lung TACs displayed a washout pattern peaking early in the imaging session (5 min for hearts and 10 min for lungs). Although not different, uptake in *ghsr*^{-/-} mice tended to washout more quickly in both cardiac and pulmonary tissue. Meanwhile, [1-Nal⁴, Lys⁵(4-[¹⁸F]-FB)]G-7039 accumulated in the abdomen in both groups and plateaued after 15 min, with non-significantly greater uptake in *ghsr*^{-/-} mice, suggesting marginally faster clearance in *ghsr*^{-/-} mice. Therefore, *in vivo* pharmacokinetics of [1-Nal⁴, Lys⁵(4-[¹⁸F]-FB)]G-7039 were independent of GHSR1a expression.

It is possible that the minimally differential uptake of [1-Nal⁴, Lys⁵(4-[¹⁸F]-FB)]G-7039 in the heart may be a function of GHSR1a expression; however, specificity could not be confirmed. While GHSR1a expression is abundant in the hearts of wt mice, we were unable to detect it using [1-Nal⁴, Lys⁵(4-[¹⁸F]-FB)]G-7039, leading us to conclude that [1-Nal⁴, Lys⁵(4-[¹⁸F]-FB)]G-7039 uptake is not a surrogate measure of GHSR1a expression. PET

dynamic images confirmed that the probe was being cleared within the first hour after injection. Signal was visible in the liver but not the kidneys, suggesting the probe was mainly excreted through the liver and intestinal system which is consistent with previous studies using a lipophilic tracer^{81,83}.

Binding of [1-Nal⁴, Lys⁵(4-FB)]G-7039 in tissues of *ghsr*^{-/-} mice can be explained by either non-specific binding, or probe reserve bound to circulating proteins. [1-Nal⁴, Lys⁵(4-FB)]G-7039 was unable to discern receptor expression even though we discovered there were differences by fluorescence microscopy. Uptake is independent of plasma ghrelin levels and, although not significant, a slight positive trend was observed when relating GHSR1a expression to cardiac uptake of [1-Nal⁴, Lys⁵(4-FB)]G-7039.

This molecule's lipophilicity causes it to be highly insoluble in conventional clinical injection vehicles (eg. saline) and contributed to non-specific binding to glass, plastic and metal surfaces. As such, it was solubilized in 100% ethanol and diluted as necessary down to <5% in saline upon injection.

4.6 Post-Mortem Tissue Staining of Metabolic Markers

Post-mortem analysis confirmed expression of GHSR1a in the fasted and fed mice, with no differences observed. Receptor expression was also confirmed in the wt mice and, unexpectedly, *ghsr*^{-/-} mice as well, with cardiac expression of GHSR1a significantly reduced, but still detectable, in *ghsr*^{-/-} mice. The fatty acid transporter CD36 has been found to bind synthetic growth hormone secretagogues (GHSs)^{108,109}, which may explain non-specific binding of Cy5-ghrelin in the *ghsr*^{-/-} mice. Even after 12 h of fasting compared to rats fed *ad libitum*, others have not noted changes to GHSR1a mRNA expression¹¹⁰. It is unknown what an appropriate fasting time would be to observe changes to cardiac GHSR1a expression. Circulating ghrelin levels are decreased in patients with HF⁷⁶ and GHSR1a levels in the heart are elevated⁷⁷, so it has been suggested that increases in GHSR1a expression are attempts to compensate for reduced ghrelin signaling. We were unable to determine any relationship between circulating ghrelin and GHSR1a expression in normal mice. Observable changes to receptor expression may only occur in a pathologic state such

that receptor expression responds to ligand availability, where expression is increased when the ligand is scarce.

Interestingly, cardiac ghrelin levels were elevated in fed mice sacrificed 1 h post-injection, while circulating levels exhibited a similar (non-significant) trend. This is unexpected because circulating ghrelin is usually elevated in a fasted state. However, ghrelin is produced and secreted locally by cardiomyocytes⁷⁴. We also found that circulating ghrelin levels were not correlated with cardiac ghrelin expression, possibly indicating that cardiac ghrelin regulation is independent of the peripheral system. The regulatory mechanisms behind cardiac ghrelin secretion are not currently understood.

The expression of the insulin-dependent glucose transporter GLUT4 was reduced in fasted mice as compared to fed. This is consistent with expectations¹¹¹, as in a fasted state insulin secretion is downregulated and ghrelin levels are elevated, further suppressing insulin secretion.

Differences were not observed in SERCA2a between wt and *ghsr*^{-/-} mice indicating that GHSR1a does not influence cytosolic Ca²⁺ handling in a healthy state. GLUT4 and CD36 expression were also unaffected in healthy *ghsr*^{-/-} mice, suggesting that the ghrelin/GHSR1a axis is not integral to metabolism in healthy hearts even under temporary fasting conditions. Prolonged fasting has been demonstrated to tease out the differences in expression of these transporters. For example, decreased GLUT4 mRNA and increased CD36 expression in rats fasted for 46 h has been reported¹¹².

In HF, ghrelin has been shown to restore cardiac energy balance by reversing the switch from lipids to glucose as the primary substrate to reflect a similar metabolic profile to that of healthy hearts¹¹³. This is possibly because one of the downstream mechanisms of GHSR1a activation is a decrease in lipid oxidation (which is present in HF)¹¹⁴. Initially switching to glucose is meant to be oxygen sparing, but under chronic conditions, it is detrimental because the metabolic demand exceeds the energy that can be supplied, particularly in an anaerobic state where glucose metabolism is uncoupled from the Krebs cycle and the electron transport chain¹⁴. We did not observe differences in ghrelin or GLUT4 between wt and *ghsr*^{-/-} mice, whereas both were elevated in fed mice; therefore, it

is possible that the ghrelin/GHSR1a axis works to maintain cardiac energy balance instead of impacting cardiac metabolism.

Imaging and biodistribution studies revealed probe uptake in the lungs of both wt and *ghsr*^{-/-} mice, so we evaluated pulmonary GHSR1a expression. Notably, again, GHSR1a expression was detected in *ghsr*^{-/-} mice. It is unknown if this is due to pulmonary expression of CD36 as this was not evaluated. Potter et al.⁸⁴ found similarly high lung uptake and postulated that this was due to lack of specific binding due to high lipophilicity, which is likely the same explanation for our findings. Aside from studies in developmental physiology in rats that showed GHSR1a expressed in lungs¹¹⁵ and cancer studies, there have also been reports of pulmonary GHSR1a expression in mice¹¹⁶. Pulmonary expression has been documented in human tissue¹¹⁷, but was much less than myocardial expression⁸⁵. There is evidence that GHSR1a is expressed in alveolar macrophages¹¹⁸, where it is thought to play a protective role. However, our histology analysis did not display presence of alveolar macrophages in either group. This leads us to believe that the lung uptake observed in this study is most likely due to non-specific distribution.

The morphology of the lung tissue appeared the same in both groups, leading to the conclusion that unstressed *ghsr*^{-/-} mice did not exhibit phenotypic differences in pulmonary structure.

4.7 Future Directions

In vitro stability experiments show that [1-Nal⁴, Lys⁵(4-[¹⁸F]-FB)]G-7039 is a stable structure over time. It should be noted that stability was tested in 25% human serum, which did not account for metabolism in the liver and other organs. *In vivo* metabolite studies testing whole blood and urine at various time-points can help to elucidate effects of clearance tissues like the liver and kidneys and can also provide indications of the types of metabolites, and clearance routes, allowing for modifications to structure to improve *in vivo* investigations.

In vitro characterization showed good binding and activation of GHSR1a, so future studies should focus on improving the probe's properties to be more of a favourable *in vivo* agent,

by generating a peptidomimetic library to elucidate possible formulations. In future developments, reducing the lipophilicity of GHSs and achieving a binding affinity in the picomolar range are important for *in vivo* implementation.

It would also be useful to model tracer kinetics *in vivo* to evaluate how the tracer binds and to generate a receptor distribution map in the heart. It would be prudent to use a larger animal model to visualize the heart (eg. rats) especially because there are established rat models of GHSR1a knockout and cardiomyopathy. Software is available to model pharmacokinetics and arterial blood can be sampled while imaging to acquire the arterial input function (AIF) to measure regional probe uptake in the heart¹¹⁹. To generate quantitative data of the probe flux: 1) from plasma to tissue, 2) association of free ligand with receptor, and 3) ligand dissociation from receptor (Figure 15) can be quantified using time activity curves from the tissue of interest and a reference region lacking the receptor. Kinetic modelling will provide an estimation of the *in vivo* binding potential of the ligand. Others have shown that graphical analysis is useful in quantifying enzymatic binding of ¹¹C-rolipram in rat myocardium, showing that it is possible to measure tracer distribution in the rodent heart¹²⁰.

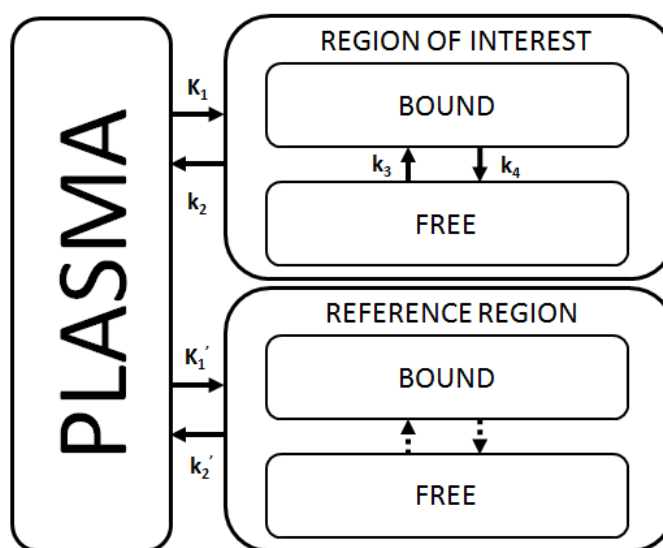


Figure 15. Compartmental model using a reference tissue to quantify probe flux.

Future experiments should also look to address differences in ghrelin levels and to potentially determine whether the ghrelin/GHSR1a axis contributes to cardiac metabolism.

In this pursuit, mice should be fasted for longer and fed mice should be fasted prior to feeding and then followed with tracer injection so that ghrelin levels are controlled for. Moreover, Cy5-ghrelin binding in *ghsr*^{-/-} mice should be addressed, by evaluating the fluorescent probe for CD36 binding. Also, binding of [1-Nal⁴, Lys⁵(4-[¹⁸F]-FB)]G-7039 to CD36 has not been evaluated, but has been reported with the synthetic GHS hexarelin, so it would be appropriate to test this.

5 Conclusions and Significance

This study provides insight into probe development for imaging GHSR1a. The PET probe [1-Nal⁴, Lys⁵(4-[¹⁸F]-FB)]G-7039 demonstrated *in vitro* stability and strong affinity for the ghrelin receptor. It was characterized *in vivo* and did not demonstrate specific accumulation in the heart. *In vitro* analysis of probe specificity determined that binding was independent of receptor expression, which was confirmed by *in vivo* studies in wt and receptor-knockout mice. *Ex vivo* biodistribution comparing specificity and effects of nutritional state showed that uptake was independent of circulating ghrelin levels induced by fasting. High uptake in the clearance pathways indicated probe elimination through hepatobiliary and renal clearance. In addition, PET imaging in wt and *ghsr*^{-/-} mice immediately post-injection was unable to discriminate receptor expression, thus specificity of [1-Nal⁴, Lys⁵(4-[¹⁸F]-FB)]G-7039 could not be confirmed.

Despite the strides made in imaging research for HF, distinguishing early pathogenesis and understanding disease mechanisms remain unsolved concerns. Advances in therapeutic approaches have emphasized the necessity for early recognition of heart failure which can improve symptoms and quality of life, reduce disease progression rates, reduce hospital admission rates, and increase survival. *Ex vivo* biodistribution and *in vivo* imaging data acquired in mice represent a step towards characterizing a suitable GHSR1a PET tracer.

References

1. Tu, J. V. *et al.* National trends in rates of death and hospital admissions related to acute myocardial infarction, heart failure and stroke, 1994–2004. *Can. Med. Assoc. J.* **180**, E118–E125 (2009).
2. Reitsma, J. B. *et al.* Increase in hospital admission rates for heart failure in The Netherlands, 1980–1993. *Heart* **76**, 388–392 (1996).
3. Tran, D. T. *et al.* The current and future financial burden of hospital admissions for heart failure in Canada: a cost analysis. *Can. Med. Assoc. J. Open* **4**, E365–E370 (2016).
4. Canadian Institute for Health Information. All-Cause Readmission to Acute Care and Return to the Emergency Department. *Heal. Syst. Perform.* 64 (2012).
5. Mozaffarian, D. *et al.* Heart Disease and Stroke Statistics – At-a-Glance Heart Disease, Stroke and other Cardiovascular Diseases Heart Disease, Stroke and Cardiovascular Disease Risk Factors. *Am. Hear. Assoc.* 7–10 (2015). doi:10.1161/CIR.000000000000152.
6. Johansen, H., Strauss, B., Arnold, J. M. O., Moe, G. & Liu, P. On the rise: The current and projected future burden of congestive heart failure hospitalization in Canada. *Can. J. Cardiol.* **19**, 430–5 (2003).
7. Association, T. C. C. of the N. Y. H. *Nomenclature and Criteria for Diagnosis of Diseases of the Heart and Great Vessels.* (Little Brown & Co, 1994).
8. Yancy, C. W. *et al.* 2013 ACCF/AHA guideline for the management of heart failure: A report of the american college of cardiology foundation/american heart association task force on practice guidelines. *Circulation* **128**, (2013).
9. Gheorghide, M. & Bonow, R. O. Heart failure Early follow-up after hospitalization for heart failure. *Nat. Rev. Cardiol.* **7**, 422–424 (2010).
10. Kemp, C. D. & Conte, J. V. The pathophysiology of heart failure. *Cardiovasc. Pathol.* **21**, 365–371 (2012).
11. Cowie, M. R. *et al.* Incidence and aetiology of heart failure; a population-based study. *Eur. Hear. J.* **20**, 421 LP-428 (1999).
12. Pecini, R., Møller, D. V., Torp-Pedersen, C., Hassager, C. & Køber, L. Heart failure etiology impacts survival of patients with heart failure. *Int. J. Cardiol.* **149**, 211–215 (2011).
13. Ashley, E. & Niebauer, J. Heart failure. *Cardiology Explained* Chapter 7 (2004). Available at: <https://www.ncbi.nlm.nih.gov/books/NBK2218/>.
14. Tham, Y. K., Bernardo, B. C., Ooi, J. Y. Y., Weeks, K. L. & McMullen, J. R. Pathophysiology of cardiac hypertrophy and heart failure: signaling pathways and novel therapeutic targets. *Arch. Toxicol.* **89**, 1401–1438 (2015).
15. Pietka, T. A. *et al.* CD36 protein influences myocardial Ca²⁺ homeostasis and phospholipid metabolism: conduction anomalies in CD36-deficient mice during

- fasting. *J. Biol. Chem.* **287**, 38901 (2012).
16. Heather, L. C. *et al.* Differential translocation of the fatty acid transporter, FAT/CD36, and the glucose transporter, GLUT4, coordinates changes in cardiac substrate metabolism during ischemia and reperfusion. *Circ.-Heart Fail.* **6**, 1058 (2013).
 17. Yeung, D. F. *et al.* Trends in the incidence and outcomes of heart failure in Ontario, Canada: 1997 to 2007. *Can. Med. Assoc. J.* **184**, E765-73 (2012).
 18. McKelvie, R. S. *et al.* The 2012 Canadian Cardiovascular Society Heart Failure Management Guidelines Update: Focus on Acute and Chronic Heart Failure. *Can. J. Cardiol.* **29**, 168–181 (2013).
 19. Maceira, A., Maceira, A., Prasad, S., Khan, M. & Pennell, D. Normalized Left Ventricular Systolic and Diastolic Function by Steady State Free Precession Cardiovascular Magnetic Resonance. *J. Cardiovasc. Magn. Reson.* **8**, 417–426 (2006).
 20. Kim, R. J. *et al.* Relationship of MRI delayed contrast enhancement to irreversible injury, infarct age, and contractile function. *Circulation* **100**, 1992–2002 (1999).
 21. Marwick, T. H. & Schwaiger, M. The future of cardiovascular imaging in the diagnosis and management of heart failure, part 1: tasks and tools. *Circ. Cardiovasc. Imaging* **1**, 58–69 (2008).
 22. Iles, L. *et al.* Evaluation of diffuse myocardial fibrosis in heart failure with cardiac magnetic resonance contrast-enhanced T1 mapping. *J. Am. Coll. Cardiol.* **52**, 1574–1580 (2008).
 23. Paterson, I., Mielniczuk, L. M., O’Meara, E., So, A. & White, J. A. Imaging Heart Failure: Current and Future Applications. *Can. J. Cardiol.* **29**, 317–328 (2013).
 24. Bhatia, R. S. *et al.* Outcome of Heart Failure with Preserved Ejection Fraction in a Population-Based Study. *New Engl. J. Med.* **355**, 260–269 (2006).
 25. Massoud, T. F. & Gambhir, S. S. Molecular imaging in living subjects: seeing fundamental biological processes in a new light. *Gene. Dev.* **17**, 545–580 (2003).
 26. James, M. L. & Gambhir, S. S. A Molecular Imaging Primer: Modalities, Imaging Agents, and Applications. *Physiol. Rev.* **92**, 897–965 (2012).
 27. Salcedo, E. E., Moloo, J., Quaife, R. & Wolfel, E. Imaging Heart Failure in 2010. *Curr. Cardiovasc. Imaging Rep.* **3**, 303–316 (2010).
 28. Di Carli, M. F. *et al.* Clinical Myocardial Perfusion PET/CT. *J. Nucl. Med.* **48**, 783–793 (2007).
 29. Tio, R. A. *et al.* Comparison Between the Prognostic Value of Left Ventricular Function and Myocardial Perfusion Reserve in Patients with Ischemic Heart Disease. *J. Nucl. Med.* **50**, 214–219 (2009).
 30. Knaapen, P. *et al.* Perfusible Tissue Index as a Potential Marker of Fibrosis in Patients with Idiopathic Dilated Cardiomyopathy. *J. Nucl. Med.* **45**, 1299 (2004).
 31. Rischpler, C., Higuchi, T. & Nekolla, S. G. Current and Future Status of PET

- Myocardial Perfusion Tracers. *Curr. Cardiovasc. Imaging Rep.* **8**, 1–9 (2015).
32. Ido, T. *et al.* Labeled 2-deoxy-D-glucose analogs. 18F-labeled 2-deoxy-2-fluoro-D-glucose, 2-deoxy-2-fluoro-D-mannose and 14C-2-deoxy-2-fluoro-D-glucose. *J. Label. Compd. Radiopharm.* **14**, 175–183 (1978).
 33. Schinkel, A. F. L. *et al.* Hibernating Myocardium: Diagnosis and Patient Outcomes. *Curr. Prob. Cardiology* **32**, 375–410 (2007).
 34. Bengel, F. M., Higuchi, T., Javadi, M. S. & Lautamäki, R. Cardiac Positron Emission Tomography. *J. Am. Coll. Cardiol.* **54**, 1–15 (2009).
 35. Langer, O. & Halldin, C. PET and SPET tracers for mapping the cardiac nervous system. *Eur. J. Nucl. Med.* **29**, 416–434 (2002).
 36. Schwaiger, M. *et al.* Noninvasive evaluation of sympathetic nervous system in human heart by positron emission tomography. *Circulation* **82**, 457–464 (1990).
 37. Caldwell, J. H., Link, J. M., Levy, W. C., Poole, J. E. & Stratton, J. R. Evidence for Pre- to Postsynaptic Mismatch of the Cardiac Sympathetic Nervous System in Ischemic Congestive Heart Failure. *J. Nucl. Med.* **49**, 234–241 (2008).
 38. Tsukamoto, T. *et al.* Decreased myocardial beta-adrenergic receptor density in relation to increased sympathetic tone in patients with nonischemic cardiomyopathy. *J. Nucl. Med.* **48**, 1777 (2007).
 39. Naya, M. *et al.* Myocardial [beta]-Adrenergic Receptor Density Assessed by 11C-CGP12177 PET Predicts Improvement of Cardiac Function After Carvedilol Treatment in Patients with Idiopathic Dilated Cardiomyopathy. *J. Nucl. Med.* **50**, 220 (2009).
 40. Wollenweber, T. & Bengel, F. M. Cardiac molecular imaging. *Semin. Nucl. Med.* **44**, 386 (2014).
 41. Narula, J. *et al.* Apoptosis in Myocytes in End-Stage Heart Failure. *New Engl. J. Med.* **335**, 1182–1189 (1996).
 42. Zhu, J.-C., Wang, F., Fang, W., Hua, Z.-C. & Wang, Z. 18F-annexin V apoptosis imaging for detection of myocardium ischemia and reperfusion injury in a rat model. *J. Radioanal. Nucl. Chem.* **298**, 1733–1738 (2013).
 43. Lehner, S. *et al.* In Vivo Monitoring of Parathyroid Hormone Treatment after Myocardial Infarction in Mice with [68Ga]Annexin A5 and [18F]Fluorodeoxyglucose Positron Emission Tomography. *Mol. Imaging* **13**, (2014).
 44. Lu, E. *et al.* Targeted in vivo labeling of receptors for vascular endothelial growth factor: approach to identification of ischemic tissue. *Circulation* **108**, 97–103 (2003).
 45. Sherif, H. M. *et al.* Molecular Imaging of Early v 3 Integrin Expression Predicts Long-Term Left-Ventricle Remodeling After Myocardial Infarction in Rats. *J. Nucl. Med.* **53**, 318–323 (2012).
 46. Makowski, M. R., Ebersberger, U., Nekolla, S. & Schwaiger, M. In vivo molecular

- imaging of angiogenesis, targeting v 3 integrin expression, in a patient after acute myocardial infarction. *Eur. Heart J.* **29**, 2201 (2008).
47. Felker, G., Petersen, J. & Mark, D. Natriuretic peptides in the diagnosis and management of heart failure. *Can. Med. Assoc. J.* **175**, 611–617 (2006).
 48. Poletti, R. *et al.* Prognostic value of plasma renin activity in heart failure patients with chronic kidney disease. *Int. J. Cardiol.* **167**, 711–715 (2013).
 49. Masson, S. *et al.* Elevated Plasma Renin Activity Predicts Adverse Outcome in Chronic Heart Failure, Independently of Pharmacologic Therapy: Data From the Valsartan Heart Failure Trial (Val-HeFT). *J. Card. Fail.* **16**, 964–970 (2010).
 50. Vergaro, G. *et al.* Prognostic Value of Plasma Renin Activity in Heart Failure. *Am. J. Cardiol.* **108**, 246–251 (2011).
 51. Gandhi, P. U. & Pinney, S. Management of chronic heart failure: Biomarkers, monitors, and disease management programs. *Ann. Glob. Heal.* **80**, 46–54 (2014).
 52. JA, D., PP, G., Pietrzak, E. & AJ, D. A systematic review of the diagnostic accuracy of natriuretic peptides for heart failure. *Arch. Intern. Med.* **164**, 1978–1984 (2004).
 53. Mehra, M. R. *et al.* Obesity and suppressed B-type natriuretic peptide levels in heart failure. *J. Am. Coll. Cardiol.* **43**, 1590–1595 (2004).
 54. Mir, T. S. *et al.* Plasma Concentrations of N-Terminal Brain Natriuretic Peptide in Healthy Children, Adolescents, and Young Adults: Effect of Age and Gender. *Pediatr. Cardiol.* **27**, 73–77 (2006).
 55. Blondé-Cynober, F. *et al.* Diagnostic and prognostic value of brain natriuretic peptide (BNP) concentrations in very elderly heart disease patients: Specific geriatric cut-off and impacts of age, gender, renal dysfunction, and nutritional status. *Arch. Gerontol. Geriatr.* **52**, 106–110 (2011).
 56. Tang, W. H. W. *et al.* Plasma B-Type Natriuretic Peptide Levels in Ambulatory Patients With Established Chronic Symptomatic Systolic Heart Failure. *Circulation* **108**, 2964 LP-2966 (2003).
 57. Wettersten, N. & Maisel, A. S. Troponin-Guided Heart Failure Therapy: Are We There Yet? *Curr. Emerg. Hosp. Med. Rep.* **4**, 200–205 (2016).
 58. Omland, T., Røsjø, H., Giannitsis, E. & Agewall, S. Troponins in heart failure. *Int. J. Clin. Chem.* **443**, 78
 59. Sato, Y., Fujiwara, H. & Takatsu, Y. Cardiac troponin and heart failure in the era of high-sensitivity assays. *J. Cardiol.* **60**, 160–167 (2012).
 60. Jungbauer, C. G., Riedlinger, J., Block, D. & Stadler, S. Panel of emerging cardiac biomarkers contributes for prognosis rather than diagnosis in chronic heart failure. *Biomark. Med.* **8**, 777–789 (2014).
 61. Klok, M. D., Jakobsdottir, S. & Drent, M. L. The role of leptin and ghrelin in the regulation of food intake and body weight in humans: A review. *Obesit. Rev.* **8**, 21–34 (2007).

62. Cummings, D. E. *et al.* A Preprandial Rise in Plasma Ghrelin Levels Suggests a Role in Meal Initiation in Humans. *Diabetes* **50**, 1714–1719 (2001).
63. Smith, R. G. *et al.* Peptidomimetic Regulation of Growth Hormone Secretion. *Endocr. Rev.* **18**, 621–645 (1997).
64. Howard, A. D. *et al.* A Receptor in Pituitary and Hypothalamus That Functions in Growth Hormone Release. *Science* **273**, 974–977 (1996).
65. Leite-Moreira, A. F., Rocha-Sousa, A. & Henriques-Coelho, T. in *Ghrelin* (ed. Hormones, B. T.-V. &) **Volume 77**, 207–238 (Academic Press, 2007).
66. Kojima, M. *et al.* Ghrelin is a growth-hormone-releasing acylated peptide from stomach. *Nature* **402**, 656–660 (1999).
67. Tesauro, M., Schinzari, F., Caramanti, M., Lauro, R. & Cardillo, C. Metabolic and Cardiovascular Effects of Ghrelin. *Life Sci.* **2010**, 261–271 (2010).
68. Baldanzi, G. *et al.* Ghrelin and des-acyl ghrelin inhibit cell death in cardiomyocytes and endothelial cells through ERK1/2 and PI 3-kinase/AKT. *J. Cell Biol.* **159**, 1029–1037 (2002).
69. Soeki, T. *et al.* Ghrelin suppresses cardiac sympathetic activity and prevents early left ventricular remodeling in rats with myocardial infarction. *Am. J. Physiol-Heart C.* **294**, 426–432
70. Nagaya, N. *et al.* Hemodynamic and hormonal effects of human ghrelin in healthy volunteers. *Am. J. Physiol-Reg. I.* **280**, 1483–1487 (2001).
71. Nagaya, N., Miyatake, K., Uematsu, M. & Oya, H. Hemodynamic, renal, and hormonal effects of ghrelin infusion in patients with chronic heart failure. *J. Clin. Endocr. Metab.* **86**, 5854–5859 (2001).
72. Mao, Y., Tokudome, T. & Kishimoto, I. The cardiovascular action of hexarelin. *J. Geriatr. Cardiol.* **11**, 253–8 (2014).
73. Müller, T. D. *et al.* Ghrelin. *Mol. Metab.* **4**, 437–460 (2015).
74. Zhang, G. *et al.* Ghrelin and Cardiovascular Diseases. *Curr. Cardiol. Rev.* **6**, 62–70 (2010).
75. Kishimoto, I., Tokudome, T., Hosoda, H., Miyazato, M. & Kangawa, K. Ghrelin and cardiovascular diseases. *J. Cardiol.* **59**, 8–13 (2012).
76. Chen, Y. *et al.* Prognostic value of plasma ghrelin in predicting the outcome of patients with chronic heart failure. *Arch. Med. Res.* **45**, 263–9 (2014).
77. Beiras-Fernandez, A. *et al.* Altered myocardial expression of ghrelin and its receptor (GHSR-1a) in patients with severe heart failure. *Peptides* **31**, 2222–8 (2010).
78. Lund, L. H. *et al.* Ghrelin resistance occurs in severe heart failure and resolves after heart transplantation. *Eur. J. Hear. Fail.* **11**, 789–794 (2009).
79. Zabarovskaja, S. *et al.* Acylation of ghrelin is increased in heart failure and decreases post heart transplantation. *Scand. Cardiovasc. J.* **48**, 343–348 (2014).

80. Katugampola, S. D., Pallikaros, Z. & Davenport, A. P. [125I- His9]- Ghrelin, a novel radioligand for localizing GHS orphan receptors in human and rat tissue; up- regulation of receptors with atherosclerosis. *Brit. J. Pharmacol.* **134**, 143–149 (2001).
81. Koźmiński, P. & Gniazdowska, E. Synthesis and in vitro/in vivo evaluation of novel mono- and trivalent technetium-99m labeled ghrelin peptide complexes as potential diagnostic radiopharmaceuticals. *Nucl. Med. Biol.* **42**, 28–37 (2015).
82. Moldovan, R.-P. *et al.* Development of Fluorinated Non-Peptidic Ghrelin Receptor Ligands for Potential Use in Molecular Imaging. *Int. J. Mol. Sci.* **18**, (2017).
83. Chollet, C., Bergmann, R., Pietzsch, J. & Beck-Sickinger, A. G. Design, evaluation, and comparison of ghrelin receptor agonists and inverse agonists as suitable radiotracers for PET imaging. *Bioconjug. Chem.* **23**, 771–84 (2012).
84. Potter, R. *et al.* Synthesis and in vivo evaluation of (S)-6-(4-fluorophenoxy)-3-((1-[11C]methylpiperidin-3-yl)methyl)-2-o-tolylquinazolin-4(3H)-one, a potential PET tracer for growth hormone secretagogue receptor (GHSR). *Bioorg. Med. Chem.* **19**, 2368–2372 (2011).
85. Papotti, M. *et al.* Growth hormone secretagogue binding sites in peripheral human tissues. *J. Clin. Endocr. Metab.* **85**, 3803–3807 (2000).
86. Douglas, G. A. F. *et al.* Characterization of a far-red analog of ghrelin for imaging GHS-R in P19-derived cardiomyocytes. *Peptides* **54**, 81–88 (2014).
87. McGirr, R., McFarland, M. S., McTavish, J., Luyt, L. G. & Dhanvantari, S. Design and characterization of a fluorescent ghrelin analog for imaging the growth hormone secretagogue receptor 1a. *Regul. Pept.* **172**, 69–76 (2011).
88. Lu, C. *et al.* Ghrelin receptor as a novel imaging target for prostatic neoplasms . *The Prostate* **72**, 825–833 (2012).
89. Rosita, D., DeWit, M. A. & Luyt, L. G. Fluorine and Rhenium Substituted Ghrelin Analogues as Potential Imaging Probes for the Growth Hormone Secretagogue Receptor. *J. Med. Chem.* **52**, 2196–2203 (2009).
90. Charlton, C. L., Dhanvantari, S. & Luyt, L. G. Evaluation of [68Ga]-DOTA ghrelin (1–19) in LNCaP prostate carcinoma. *Nucl. Med. Biol.* **41**, 638 (2014).
91. Powell, M. F. *et al.* Peptide stability in drug development. II. Effect of single amino acid substitution and glycosylation on peptide reactivity in human serum. *Pharm. Res.* **10**, 1296–1273 (1993).
92. Patterson, Z. R., Ducharme, R., Anisman, H. & Abizaid, a. Altered metabolic and neurochemical responses to chronic unpredictable stressors in ghrelin receptor-deficient mice. *Eur. J. Neurosci.* **32**, 632–9 (2010).
93. Visser, E. P. *et al.* Spatial Resolution and Sensitivity of the Inveon Small-Animal PET Scanner. *J. Nucl. Med.* **50**, 139–147 (2009).
94. Goertzen, A. L. *et al.* NEMA NU 4-2008 comparison of preclinical PET imaging systems. *J. Nucl. Med.* **53**, 1300–1309 (2012).

95. Puntorieri, V., McCaig, L. A., Howlett, C. J. & Yao, L.-J. Lack of matrix metalloproteinase 3 in mouse models of lung injury ameliorates the pulmonary inflammatory response in female but not in male mice. *Exp. Lung Res.* **42**, 365–379 (2016).
96. McGirr, R., Guizzetti, L. & Dhanvantari, S. The sorting of proglucagon to secretory granules is mediated by carboxypeptidase E and intrinsic sorting signals. *J. Endocrinol.* **217**, 229–240 (2013).
97. Fowkes, M. M. Peptidomimetic GHS-R1a Agonists as PET Imaging Agents for Prostate Cancer. (2014).
98. Ishiwata, K., Kimura, Y., de Vries, E. F. & Elsinga, P. H. PET Tracers for Mapping Adenosine Receptors as Probes for Diagnosis of CNS Disorders. *Cent. Nerv. Syst. Agents Med. Chem.* **7**, 57–77(21) (2007).
99. Arnott, J. A. & Planey, S. L. The influence of lipophilicity in drug discovery and design. *Expert Opin. Drug Discov.* **7**, 863–875 (2012).
100. Patrick, G. L. An introduction to medicinal chemistry. 87 (2015).
101. Thompson, S. J., Hattotuagama, C. K., Holliday, J. D. & Flower, D. R. On the hydrophobicity of peptides: Comparing empirical predictions of peptide log P values. *Bioinformatics* **1**, 237 (2006).
102. De Vriese, C. *et al.* Ghrelin Degradation by Serum and Tissue Homogenates: Identification of the Cleavage Sites. *Endocrinology* **145**, 4997–5005 (2004).
103. Cone, R. D., Cowley, M. A., Butler, A. A. & Fan, W. The arcuate nucleus as a conduit for diverse signals relevant to energy homeostasis. *Int. J. Obes. Relat. Metab. Disord.* **25**, S67 (2001).
104. Staes, E. *et al.* Acylated and unacylated ghrelin binding to membranes and to ghrelin receptor: Towards a better understanding of the underlying mechanisms. *BBA - Biomembranes* **1798**, 2102–2113 (2010).
105. Zigman, J. M., Jones, J. E., Lee, C. E., Saper, C. B. & Elmquist, J. K. Expression of ghrelin receptor mRNA in the rat and the mouse brain. *J. Comp. Neurol.* **494**, 528–548 (2006).
106. Zhao, T.-J. *et al.* Ghrelin secretion stimulated by β 1-adrenergic receptors in cultured ghrelinoma cells and in fasted mice. *P. Natl. A. Sci. USA* **107**, 15868–15873 (2010).
107. Lin, J. H. & Lu, A. Y. Role of pharmacokinetics and metabolism in drug discovery and development. *Pharmacol. Rev.* **49**, 403 (1997).
108. Cao, J.-M., Ong, H. & Chen, C. Effects of ghrelin and synthetic GH secretagogues on the cardiovascular system. *Trends Endocrin. Met.* **17**, 13–18 (2006).
109. Bodart, V. *et al.* CD36 Mediates the Cardiovascular Action of Growth Hormone-Releasing Peptides in the Heart. *Circ. Res.: J. Am. Heart Assoc.* **90**, 844–849 (2002).
110. Castro, H., Pomar, C. A., Picó, C., Sánchez, J. & Palou, A. Cafeteria diet

- overfeeding in young male rats impairs the adaptive response to fed/fasted conditions and increases adiposity independent of body weight. *Int. J. Obesity* **39**, 430–437 (2015).
111. Karnieli, E. & Armoni, M. Transcriptional regulation of the insulin-responsive glucose transporter GLUT4 gene: from physiology to pathology. *AJP - Endocrin. Metab.* **295**, E38–E45 (2008).
 112. Van der Lee, K. A., Willemsen, P. H., Samec, S. & Seydoux, J. Fasting-induced changes in the expression of genes controlling substrate metabolism in the rat heart. *J. Lipid Res.* **42**, 1752–1758 (2001).
 113. Mitacchione, G. *et al.* The Gut Hormone Ghrelin Partially Reverses Energy Substrate Metabolic Alterations in the Failing Heart. *Circ. Heart Fail.* **7**, 643–651 (2014).
 114. Wortley, K. E. *et al.* Genetic Deletion of Ghrelin Does Not Decrease Food Intake but Influences Metabolic Fuel Preference. *P. Natl. A. Sci. USA* **101**, 8227–8232 (2004).
 115. Nunes, S., Nogueira-Silva, C., Dias, E., Moura, R. S. & Correia-Pinto, J. Ghrelin and obestatin: Different role in fetal lung development? *Peptides* **29**, 2150–2158 (2008).
 116. Sun, Y., Garcia, J. M. & Smith, R. G. Ghrelin and Growth Hormone Secretagogue Receptor Expression in Mice during Aging. *Endocrinology* **148**, 1323–1329 (2007).
 117. Volante, M. *et al.* Ghrelin Expression in Fetal, Infant, and Adult Human Lung. *Journal of Histochemistry and Cytochemistry* **50**, 1013–1021 (2002).
 118. Li, B. *et al.* Ghrelin Protects Alveolar Macrophages Against Lipopolysaccharide-Induced Apoptosis Through Growth Hormone Secretagogue Receptor 1a-Dependent c-Jun N-Terminal Kinase and Wnt/ β -Catenin Signaling and Suppresses Lung Inflammation. *Endocrinology* **156**, 203–217 (2015).
 119. Alf, M. F. *et al.* Quantification of brain glucose metabolism by ^{18}F -FDG PET with real-time arterial and image-derived input function in mice. *J. Nucl. Med.* **54**, 132–8 (2013).
 120. Thomas, A. J. *et al.* PET of (R)- ^{11}C -Rolipram Binding to Phosphodiesterase-4 Is Reproducible and Sensitive to Increased Norepinephrine in the Rat Heart. *J. Nucl. Med.* **52**, 263 (2011).

Appendices

Appendix A. [1-Nal⁴, Lys⁵(4-[¹⁸F]-FB)]G-7039 Pre-SOP synthesis method

All the reagents and solvents used for radiosynthesis were purchased from Sigma-Aldrich unless otherwise stated. ¹⁸F-fluoride was produced via the ¹⁸O(p,n) ¹⁸F reaction in a GE PETtrace 880 cyclotron at Lawson Health Research Institute for desired radiotracer synthesis. GE Tracer Lab FXN was used to prepare and purify [¹⁸F]fluorobenzoic Acid ([¹⁸F]FBA) Post-SOP.

As described in Scheme 1, [¹⁸F]FBA was prepared manually. Aqueous [¹⁸F]fluoride solution was trapped on the Sep-Pak AccellTM plus carbonated QMA light cartridge. 1 mL of acetonitrile/H₂O (80/20; v/v) solution containing potassium carbonate (0.0015mmol, 2.5 equivalents) and kryptofix 2.2.2 (0.016mmol, 2.8 equivalents) was used to elute [¹⁸F]fluoride into the reaction vial (Scheme 1ai). The solvent was removed azeotropically in vacuum under the helium flow at 50°C. [¹⁸F]fluoride was dried three times by adding 1 mL of anhydrous acetonitrile respectively under the above condition. 400 μL of anhydrous DMSO containing 0.0057 mmol, 1.9 equivalents mg of 4-(*Tert*-butoxycarbonyl)-*N,N,N*-trimethylbenzenammonium triflate salt was added into dried [¹⁸F]F⁻ under helium atmosphere (Scheme 1aii). The reaction vial was sealed and heated at 120°C for 10 min. At the same temperature and conditions, 1 mL of aqueous HCl (5 M) was added into reaction vial and allowed to react for 5 min. The reaction mixture was heated 3 min at 100°C for hydrolysis of ester and then cooled down to 40°C. 2.5 mL of H₂O was added to dilute the reaction mixture. The product was trapped on Sep-Pak C18 light cartridge (Waters), pre-treated with 10 mL ethanol then 10 mL water, and washed with 2 mL of H₂O.

The solution of [¹⁸F]FBA in 500 μL mL of acetonitrile was added into the vial containing 0.17 mmol NHS (*N*-Hydroxysuccinimide) and 0.23 mmol EDC (1-Ethyl-3-(3-dimethylaminopropyl)carbodiimide). The reaction was performed at room temperature for 10 min and. 1 mL of 25-90% acetonitrile/H₂O + 0.1% TFA mixture was added into the reaction vial. The raw product was purified on semipreparative HPLC column. The solvent

was removed at 36°C on V-10 evaporator to get dried [¹⁸F]SFB (46.5% radiochemical yield, radiochemical purity >99%).

The solution of 9.29e-4 mmol, 1.0 equivalent mg of [1-Nal⁴]G-7039 in 100 μL acetonitrile and 100 μL H₂O was added into the above [¹⁸F]SFB vial and followed by the addition of 5 μL DIPEA (*N,N*-Diisopropylethylamine) (Scheme 1c). The reaction mixture was heated at 50-70 °C for 15 min. 200 ul DMF, 400 uL H₂O, and 100 ul acetonitrile μL H₂O were added into reaction vial after cooling down to room temperature. The reaction mixture was purified in semipreparative column (25-90% acetonitrile + 0.1% TFA) to get [1-Nal⁴, Lys⁵(4-[¹⁸F]-FB)]G-7039 (Radiochemical yield 52%, radiochemical purity >98% and molar activity 116 MBq/μmol).

Appendix B. Pre-SOP synthesis and biodistribution results

Pre-SOP synthesis

Using the Pre-SOP synthesis method yielded [1-Nal⁴, Lys⁵(4-[¹⁸F]-FB)]G-7039 with a radiochemical yield of 29-63% (average 52%), a radiochemical purity of >98% and a molar activity of 116 MBq/μmol after 140 min.

Biodistributions using Pre-SOP synthesis

Biodistribution pre-SOP is shown in Figure 16. In fasted mice, heart uptake of [1-Nal⁴, Lys⁵(4-[¹⁸F]-FB)]G-7039 was highest in mice sacrificed 1 h and 4 h post-injection. At 1 h uptake was 6.9 ± 2.7 %ID/g, which was equivalent to the 4 h uptake of 6.9 ± 2.6 %ID/g. Heart uptake in fasted mice sacrificed 2 h post-injection was lower than animals sacrificed 1 h and 4 h post-injection (5.7 ± 3.1 %ID/g in 2 h). Only one animal was sampled for fed 2 h uptake prior to changeover to the automated synthesis protocol, so a comparison could not be made between fasted and fed groups for Pre-SOP synthesis. Therefore, it was resolved that fasting mice prior to imaging and imaging within the first hour after probe injection would be appropriate.

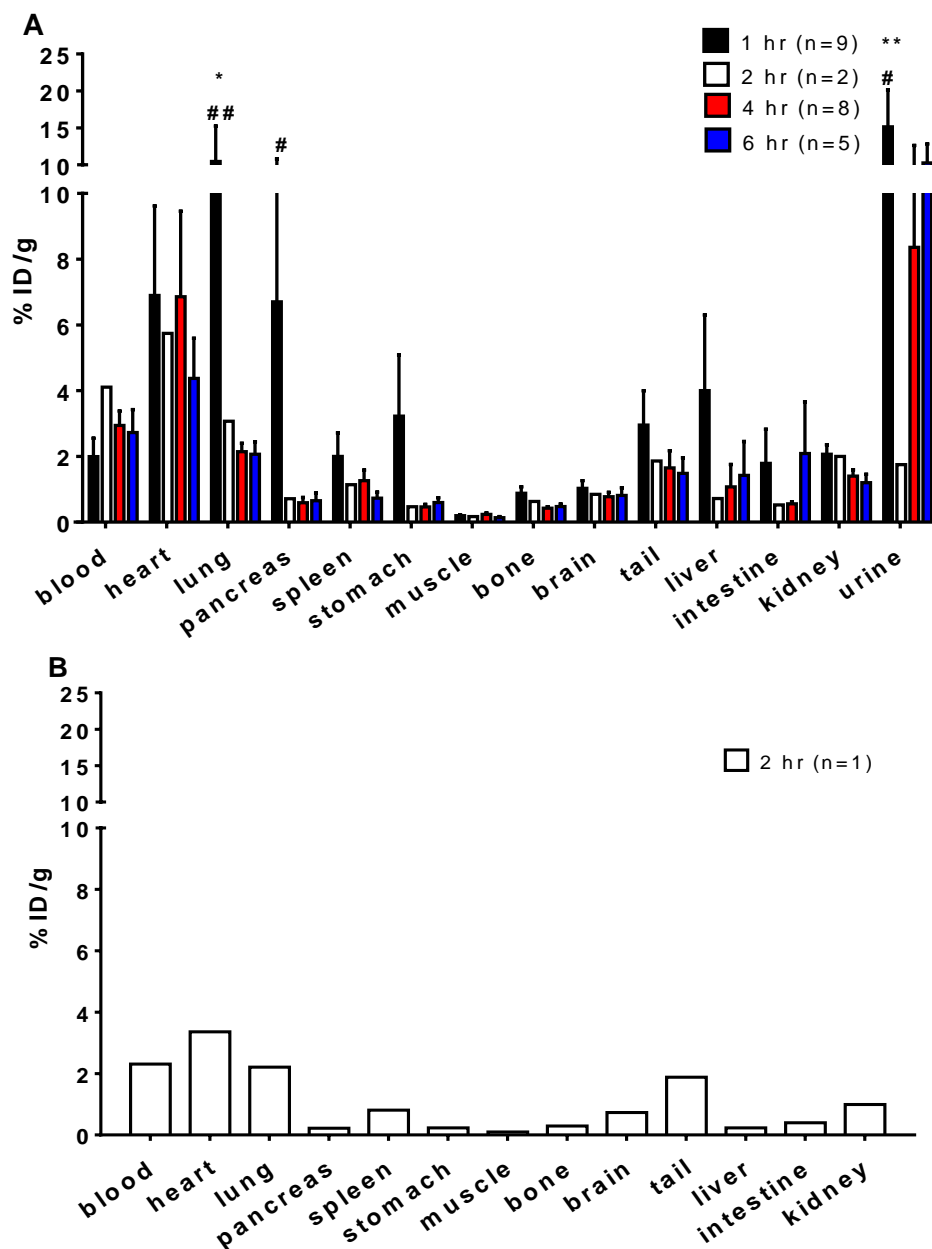


Figure 16. Biodistribution of [1-Nal⁴, Lys⁵(4-[¹⁸F]-FB)]G-7039 using Pre-SOP synthesis method in female C57BL/6 mice

Fasted (**A**) mice were euthanized 1 h, 2 h, 4 h, and 6 h after injection with [1-Nal⁴, Lys⁵(4-[¹⁸F]-FB)]G-7039. One fed (**B**) mouse was sampled at 2 h post-injection. Values are mean %ID/g \pm SEM for each group. As shown in (**A**): * p <0.05 in lung vs all tissues (except liver, pancreas and urine). ** p <0.01 urine vs all tissues, # p <0.05 in pancreas at 1 h vs 4 h, and urine at 1 h vs 2 h, ## p <0.01 in lungs at 1 h vs 4 h and 6h.

Appendix C. Animal research ethics approval

----- Forwarded Message -----

Subject: Sirius Notification - New Animal Use Protocol is APPROVED 2015-041::1

Date: Wed, 04 Nov 2015 15:56:14 -0500

From: eSiriusWebServer [REDACTED]

To: [REDACTED]

CC: [REDACTED]



AUP Number: 2015-041

PI Name: Dhanvantari, Savita

AUP Title: Development Of Ghrelin Receptor Probes For Imaging Heart Disease

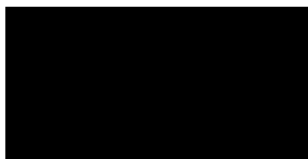
Approval Date: 11/04/2015

Official Notice of Animal Use Subcommittee (AUS) Approval: Your new Animal Use Protocol (AUP) entitled "Development Of Ghrelin Receptor Probes For Imaging Heart Disease" has been APPROVED by the Animal Use Subcommittee of the University Council on Animal Care. This approval, although valid for four years, and is subject to annual Protocol Renewal. 2015-041::1

1. This AUP number must be indicated when ordering animals for this project.
2. Animals for other projects may not be ordered under this AUP number.
3. Purchases of animals other than through this system must be cleared through the ACVS office. Health certificates will be required.

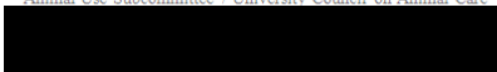
The holder of this Animal Use Protocol is responsible to ensure that all associated safety components (biosafety, radiation safety, general laboratory safety) comply with institutional safety standards and have received all necessary approvals. Please consult directly with your institutional safety officers.

Submitted by: Copeman, Laura
on behalf of the Animal Use Subcommittee



University Council on Animal Care

The University of Western Ontario
Animal Use Subcommittee / University Council on Animal Care



Appendix D. Primer pairs for genotyping GHSR1a

Wildtype Forward: 5'-CCG AGA GGA ACC ACT GAT CT-3'

Wildtype Reverse: 5'-GAT GCC AGT GGG GAC ATT AG-3'

Primers gave a 329 bp band

LacZ Forward: 5'-GTG GTG GTT ATG CCG ATC-3'

LacZ Reverse: 5'-TAC CAC AGC GGA TGG TTC GG-3'

Primers gave a 385 bp band

Curriculum Vitae

Name: Ahmed Abbas

Post-secondary Education and Degrees: **Master's of Science**
 Medical Biophysics (Molecular Imaging)
 The University of Western Ontario
 London, Ontario, Canada
 2015-2017

Bachelor's of Medical Science
 Honours Specialization Medical Biophysics (Medical Science Concentration)
 University of Western Ontario
 London, Ontario, Canada
 2011-2015

Honours and Awards: **Canada Institutes of Health Research (CIHR) Canada Graduate Scholarship – Masters**
 The University of Western Ontario
 2016-2017

Province of Ontario Graduate Scholarship (Declined)
 The University of Western Ontario
 2016-2017

Province of Ontario Graduate Scholarship
 The University of Western Ontario
 2015-2016

Western Graduate Research Scholarship
 The University of Western Ontario
 2015-2017

Western Scholar
 The University of Western Ontario
 2011-2012
 2013-2015

Dean's Honor List
 The University of Western Ontario
 2011-2015

Western University Scholarship of Excellence

The University of Western Ontario
2011-2012

**Related Work
Experience**

Graduate Research Assistant
(Supervised by Dr. Savita Dhanvantari)
The University of Western Ontario
2015-Present

Summer Research Assistant
(Supervised by Dr. Savita Dhanvantari)
Lawson Health Research Institute Imaging Program
London, Ontario, Canada
2015

Publications:

1. **Abbas A**, Beamish C, McGirr R et al. Characterization of 5-(2-¹⁸F-fluoroethoxy)-L-tryptophan for PET imaging of the pancreas. *F1000Research* 2016, 5:1851 (doi: 10.12688/f1000research.9129.2)
2. McMillan A, Dell M, Zellar MP, Cribby S, Martz S, Hong E, Fu F, **Abbas A**, Dang T, Miller W, Reid G. Disruption of urogenital biofilms by lactobacilli. *Colloids and Surfaces B: Biointerfaces* 2011, 86:1, 58-64 (doi: 10.1016/j.colsurfb.2011.03.016)

Presentations and Abstracts:

2016/09
Abbas A, Sullivan R, Lalonde T, Yu L, Charron C, Kiaii B, Wisenberg G, Luyt LG, Dhanvantari S. Imaging cardiac GHSR in situ in humans and in vivo in mice. Poster presentation at the 2016 World Molecular Imaging Congress, New York City, NY

2016/03
Abbas A, Yu L, Charron C, Lalonde T, Luyt LG, Dhanvantari S. Characterizing Positron Emission Tomography Probes for Targeting GHS-R1a as a Biomarker for Heart Failure. Poster presentation at the 2016 London Health Research Day, London, ON

2015/09
Abbas A, Demarco J, McGirr R, Hadway J, Cockburn N, Kovacs M, Krokowski D, Hatzoglou M, Dhanvantari S*. PET Imaging of Beta Cell Endoplasmic Reticulum Stress using 5-(2-¹⁸F-Fluoroethoxy)-L-Tryptophan. Podium presentation at the 2015 World Molecular Imaging Congress, Honolulu, HI
(*Presenting author)

2015/04

Abbas A, McGirr R, Hadway J, Cockburn N, Kovacs M, Krokowski D, Hatzoglou M, Dhanvantari S. PET Imaging of Beta Cell Endoplasmic Reticulum Stress using 5-(2-¹⁸F-Fluoroethoxy)-L-Tryptophan. Poster presentation at the 2015 London Health Research Day (Judged in Top 80), London, ON

2014/03

Abbas A, Guiraudon GM, Campbell G, Jones D. A Preliminary Investigation into the Effects of Various Introducers on Phantom Heart Dynamics. Class oral presentation for Medical Biophysics 3970Z Six Week Research Project, London Ontario

2010/03

Abbas A, Dang T, Fu F, Hong E, Cribby S, Miller W. Investigating the Use of Probiotic in the Treatment of Bacterial Vaginosis. Podium and poster presentations at the 2010 Sanofi-Aventis BioTalent Challenge, London, ON

2009/03

Abbas A, Hong E, Haffie T. Comparing the Effects of Various Anti-Bacterial Solution on E. Coli. Podium and poster presentations at the 2009 Sanofi-Aventis BioTalent Challenge, London, ON

Teaching Experience:

2016/09 – 2016/12

Graduate Teaching Assistant

Medical Biophysics 3501F: Biophysics of Transport Systems

2017/01 – 2017/05

Medical Biophysics 9674B: Pedagogy in Biophysics

Learned and applied pedagogical concepts to design a course in a team

2015/09 – 2017/07

Certificate in University Teaching and Learning